



Martínez-Botí, M. A., Foster, G. L., Chalk, T. B., Rohling, E. J., Sexton, P. F., Lunt, D. J., ... Schmidt, D. N. (2015). Plio-Pleistocene climate sensitivity evaluated using high-resolution CO₂ records. *Nature*, 518(7537), 49-54. <https://doi.org/10.1038/nature14145>

Peer reviewed version

Link to published version (if available):
[10.1038/nature14145](https://doi.org/10.1038/nature14145)

[Link to publication record in Explore Bristol Research](#)
PDF-document

University of Bristol - Explore Bristol Research

General rights

This document is made available in accordance with publisher policies. Please cite only the published version using the reference above. Full terms of use are available:
<http://www.bristol.ac.uk/pure/about/ebr-terms>

1 Plio-Pleistocene climate sensitivity from a new high-resolution CO₂ record

2 M.A. Martinez-Boti^{1,a}, G.L. Foster^{1,a*}, T. B. Chalk¹, E.J. Rohling^{2,1}, P.F. Sexton³, D.J. Lunt^{4,5}, R.D.
3 Pancost^{5,6}, M.P.S. Badger^{5,6}, D.N. Schmidt^{5,7}

4 ¹Ocean and Earth Science, University of Southampton, National Oceanography Centre Southampton,
5 Southampton, SO14 3ZH, UK

6 ²Research School of Earth Sciences, The Australian National University, Canberra 2601, Australia

7 ³Centre for Earth, Planetary, Space & Astronomical Research, The Open University, Milton Keynes, MK7 6AA,
8 UK

9 ⁴School of Geographical Sciences, University of Bristol, University Road, Bristol, BS8 1SS, UK

10 ⁵The Cabot Institute, University of Bristol, UK

11 ⁶Organic Geochemistry Unit, School of Chemistry, University of Bristol, BS8 1SS, UK

12 ⁷School of Earth Sciences, University of Bristol, Wills Memorial Building, Bristol, BS8 1RJ, UK

13 *corresponding author

14 ^a These authors contributed equally to this work.

15 **Theory and climate modelling suggest that the sensitivity of Earth's climate to changes in radiative**
16 **forcing could depend on background climate. However, palaeoclimate data have thus far been**
17 **insufficient to provide a conclusive test of this prediction. Here we present new atmospheric CO₂**
18 **reconstructions based on multi-site boron-isotope records through the late Pliocene (3.3 to 2.3**
19 **Myr ago). We find that Earth's climate sensitivity to CO₂-based radiative forcing (Earth System**
20 **Sensitivity) was half as strong during the warm Pliocene as during the cold late Pleistocene (0.8 to**
21 **0 Myr ago). We attribute this difference to the radiative impacts of continental ice-volume**
22 **changes (ice-albedo feedback) during the late Pleistocene, because equilibrium climate sensitivity**
23 **is identical for the two intervals when we account for such impacts using sea-level reconstructions.**

24 **We conclude that, on a global scale, no unexpected climate feedbacks operated during the warm**
25 **Pliocene, and that predictions of equilibrium climate sensitivity (excluding long-term ice-albedo**
26 **feedbacks) for our Pliocene-like future (with CO₂ levels up to maximum Pliocene levels of 450**
27 **ppm) are well described by the currently accepted range of 1.5 to 4.5 K per CO₂ doubling.**

28 Since the start of the industrial revolution, the concentration of atmospheric CO₂ (and other
29 greenhouse gases; GHGs) has increased dramatically (from ~280 to ~400 ppm)¹. It has been known
30 for over 100 years that changes in GHG concentration will cause the surface temperature of the
31 Earth to vary². A wide range of observations reveals that the sensitivity of Earth's surface
32 temperature to radiative forcing amounts to ~3 K warming per doubling of atmospheric CO₂
33 concentration (with a 66% confidence range of 1.5 to 4.5 K; e.g. ref. 1,3), due to direct radiative
34 forcing by CO₂ plus the action of a number of fast-acting positive feedback mechanisms, mainly
35 related to atmospheric water vapour content and sea-ice and cloud albedo. Uncertainty in the
36 magnitude of these feedbacks confounds our ability to determine the exact equilibrium climate
37 sensitivity (ECS; the equilibrium global temperature change for a doubling of CO₂ on timescales of
38 about a century, when all 'fast' feedbacks have had time to operate; see ref. 3 for more detail).
39 Although the likely range of values for ECS is 1.5 to 4.5 K per CO₂ doubling, there is a small but finite
40 possibility that climate sensitivity may exceed 5 K (e.g. ref. 1). Understanding the likely value of ECS
41 clearly has important implications for the magnitude, eventual impact and potential mitigation of
42 future climate change.

43 Any long-range forecast of global temperature (i.e. beyond the next 100 years) must also consider
44 the possibility that ECS could depend on the background state of the climate^{4,5}. That is, in a warmer
45 world, some feedbacks that determine ECS could become more efficient and/or new feedbacks
46 could become active to give additional warmth for a given change in radiative forcing (such as those
47 relating to methane cycling⁶, atmospheric water vapour concentrations^{5,7,8}, in addition to changes in
48 the relative opacity of CO₂ to long wave radiation^{5,9}). One approach to identify whether ECS depends

49 on climate background state is to reconstruct ECS during periods in the geological past when Earth
50 was warmer than today.

51 The Pliocene (2.6 to 5.3 Myr ago) is one such time, with the warmest intervals between 3.0 and 3.3
52 Myr ago ~ 3 K globally warmer than pre-industrial times^{10,11}, while mean sea level stood 12-32 m
53 above the present level^{12,13}. Although most of this warmth is commonly ascribed to increased
54 atmospheric CO₂ levels¹⁴, it has been suggested that simple comparisons of the observed
55 temperature change in the geological record with the climate forcing from CO₂ alone are unable to
56 constrain ECS¹⁰. Instead, a parameter termed Earth System Sensitivity (ESS) is defined – the change
57 in global temperature for a doubling of CO₂ once both fast and slow feedbacks have acted and the
58 whole Earth system has reached equilibrium (in contrast, ECS excludes the slow feedbacks; for a
59 discussion of fast versus slow feedbacks, see ref. 3). The most important slow feedbacks are those
60 related to ice-albedo and vegetation-albedo changes. Because of these slow feedbacks, Pliocene ESS
61 is thought to have been ~ 50 % higher than ECS^{10,15}, with some existing geological data suggesting a
62 Pliocene ESS range of 7-10 K per CO₂ doubling¹⁶, which greatly exceeds a modern ESS estimate of ~ 4
63 K per CO₂ doubling¹⁰. If ECS was similarly enhanced, then that would imply that either extra positive
64 fast feedbacks operated, or that existing positive fast feedbacks were more efficient, thus increasing
65 the temperature response for a given level of CO₂ forcing.

66 Understanding past climate sensitivity critically depends on the accuracy of the CO₂ data used.
67 Despite a tendency toward increased agreement between different CO₂ proxies¹⁷, individual pCO₂
68 estimates for the Pliocene still range from ~ 190 to ~ 440 μatm (Fig 1a,b) and there is little coherence
69 in the trends described by the various techniques (Fig 1a,b). This hinders any effort to accurately
70 constrain Pliocene ECS or ESS. To better determine Pliocene CO₂ levels, we generated a new record,
71 based on the boron isotopic composition ($\delta^{11}\text{B}$) of the surface mixed-layer dwelling planktic
72 foraminiferal species *Globigerinoides ruber* from ODP Site 999 (Caribbean Sea, 12°44.64' N,
73 78°44.36' W, 2838 m water depth; Extended Data Figure 1) at more than 3 \times higher temporal

74 resolution (1 sample every ~13 kyr; Fig. 1c) than previous $\delta^{11}\text{B}$ records (1 sample every 50 kyr; Fig.
75 1b). The $\delta^{11}\text{B}$ of *G. ruber* is a well-constrained function of pH^{18} and seawater pH is well correlated
76 with $[\text{CO}_2]_{\text{aq}}$, as both are a function of the ratio of alkalinity to total dissolved carbon in seawater. In
77 the absence of significant changes in surface hydrography, $[\text{CO}_2]_{\text{aq}}$ is largely a function of
78 atmospheric CO_2 levels and $\delta^{11}\text{B}$ -derived CO_2 has been demonstrated to be an accurate recorder of
79 atmospheric CO_2 (Extended Data Figure 2a)¹⁸⁻²⁰. Today, the surface water at Site 999 is close to
80 equilibrium with the atmosphere with respect to CO_2 (expressed here as $\Delta\text{pCO}_2 = \text{pCO}_2^{\text{sw}} - \text{pCO}_2^{\text{atm}} =$
81 $+21 \mu\text{atm}$; Extended Data Figure 1)^{18,21} and has remained so for at least the last 130 kyr (Extended
82 Data Figure 2)¹⁸. ODP Site 999 also benefits from a detailed astronomically calibrated age model²²
83 and high abundance of well-preserved planktic foraminifera throughout the past 4 million years^{23,24}.
84 During our study interval it is also unlikely to have been influenced by long-term oceanographic
85 changes such as the emergence of the Panama Isthmus ~3.5 Myr ago (see detailed discussion in ref.
86 23). To increase confidence that atmospheric CO_2 changes are driving our pH (and hence our pCO_2^{sw})
87 record for ODP Site 999 and that the air:sea CO_2 disequilibrium remained similar to modern values,
88 we also present lower-resolution $\delta^{11}\text{B}$ data from *G. ruber* from ODP Site 662 (equatorial Atlantic, Fig.
89 1c; $1^\circ 23.41'\text{S}$, $11^\circ 44.35'\text{W}$, 3821 m water depth; Extended Data Figure 1), where current mean
90 annual ΔpCO_2 is $+29 \mu\text{atm}$ with a seasonal maximum of $+41 \mu\text{atm}^{21}$. Analytical methodology and
91 information detailing precisely how pCO_2^{sw} is calculated, with full propagation of uncertainties, can
92 be found in the Methods section (with full $\delta^{11}\text{B}$ and pCO_2 in Supplementary Information Tables 1&2).
93

94 **A new record of Pliocene pCO_2 change**

95 Where our data for both sites overlap in time, reconstructed $\text{pCO}_2^{\text{atm}}$ values between 2.3 and 3.3
96 Myr ago agree within uncertainty (Fig 1d; Extended Data Figure 3), and are consistent with most
97 independent records (see Fig 1a,b; Extended Data Figure 2b,c), confirming that the variations we
98 observe are predominantly driven by changes in atmospheric CO_2 concentrations. However, the

99 enhanced resolution of our $\delta^{11}\text{B-pCO}_2^{\text{atm}}$ record (Fig. 1d) also reveals a hitherto
100 undocumented^{16,23,25,26} level of structure in the CO_2 variability during the 1 million year period
101 investigated, including a transition centred on 2.8 Ma, spanning ~ 200 kyr, where average $\text{pCO}_2^{\text{atm}}$
102 undergoes a decrease of ~ 65 μatm (Fig 1d).

103 Detailed atmospheric CO_2 measurements from ice cores show orbital-scale (~ 100 kyr) oscillations in
104 $\text{pCO}_2^{\text{atm}}$ with a peak-to-trough variation of ~ 80 - 100 μatm through the late Pleistocene (90 % of the
105 pCO_2 values lie between $+36$ and -41 μatm of the long-term mean; Extended Data Figures 2, 4)²⁷⁻²⁹.
106 Once the long-term trend is removed from our Plio-Pleistocene data (thick blue line in Fig 1d), and
107 we have taken into account our larger analytical uncertainty (see Methods), we observe orbital-scale
108 variations in our $\delta^{11}\text{B-pCO}_2^{\text{atm}}$ record of only slightly smaller amplitude than the ice-core $\text{pCO}_2^{\text{atm}}$
109 record (0-0.8 Myrs) and for the last 2 Myrs in other $\delta^{11}\text{B}$ -based records^{19,20,30} (Extended Data Figure 4
110 and Methods), which is in clear contrast with the benthic $\delta^{18}\text{O}$ which shows increasing variability
111 over the last 3 Myrs (Fig 1e and Extended Data Figure 4).

112 Given the different amplitudes of climate variability, the observed similarity between Pliocene and
113 late Pleistocene $\text{pCO}_2^{\text{atm}}$ variability seems counter-intuitive given the notion that CO_2 is a key factor
114 in amplifying glacial-interglacial climate change^{27-29,31,32}. This is illustrated by a well-defined non-
115 linear relationship in a cross plot between deep-sea benthic $\delta^{18}\text{O}$ and $\ln(\text{CO}_2/\text{C}_0)$ (where C_0 = pre-
116 industrial $\text{CO}_2 = 278$ μatm), which accounts for the logarithmic nature of the climate forcing by CO_2
117 (Fig. 2b). Note also the clear overlap between Pleistocene (0-2.2 Myrs) ice-core CO_2 measurements
118 and $\delta^{11}\text{B}$ -based CO_2 reconstructions in this plot (Fig. 2b; Extended Data Figure 2). A similar
119 relationship is also evident in raw $\delta^{11}\text{B}$ -space (Fig. 2a). Below an inflection at about 275 ± 15 μatm
120 $\text{pCO}_2^{\text{atm}}$ (equating to $\ln(\text{CO}_2/\text{C}_0) \approx 0$) benthic $\delta^{18}\text{O}$ shows a steeper relationship with CO_2 -based
121 forcing than it does above this value (Fig. 2). This likely reflects some combination of: (i) growth of
122 larger northern hemisphere ice sheets at $\text{pCO}_2^{\text{atm}}$ below 275 ± 15 μatm ³³ increasing radiative ice-
123 albedo feedback and amplifying climate forcing by CO_2 change; (ii) an increase in oxygen isotope

124 fractionation in precipitation with increasing size of the ice sheets, which leads to a proportionally
125 greater ^{18}O enrichment in seawater³⁴; and (iii) potentially stronger deep-sea cooling at low $\text{pCO}_2^{\text{atm}}$
126 due to the high-latitude-focussed influences of the ice-albedo feedback process. These findings
127 highlight the profound impacts of northern hemisphere ice-sheet growth on climate variability in the
128 Pleistocene^{31,32}, relative to the Pliocene (Fig. 2b).

129 Our new data show that the $\sim 275 \pm 15 \mu\text{atm}$ threshold was first crossed at $\sim 2.8 \text{ Ma}$ during Marine
130 Isotope Stage (MIS) G10 (Fig. 1d, horizontal dashed line), and – more persistently – during
131 subsequent Marine Isotope Stages G6 (2.72 Myr ago), G2 (2.65 Myr ago), and 100 (2.52 Myr ago),
132 when values as low as $233_{-53}^{+63} \mu\text{atm}$ (95% confidence) were reached and when intervening
133 interglacial values also seem to have been suppressed (Fig. 1c,d). These isotope stages are significant
134 in that they are associated with an increase in the amplitude of glacial-interglacial sea-level
135 oscillations (Extended Data Figure 5b)^{12,13,35} and coincide with the timing of the first substantial
136 continental glaciations of Europe, North America and the Canadian Cordillera, as reconstructed by
137 ice-rafted debris and observations of relic continental glacial deposits³⁶⁻³⁸. Hence, our new high-
138 resolution $\text{pCO}_2^{\text{atm}}$ record robustly confirms previous hypotheses^{16,23,25,39} (based on low-resolution
139 CO_2 data) that the first substantial stages of glaciation on the northern hemisphere, as well as a
140 recently recognised deep-sea cooling during the late Pliocene/early Pleistocene¹³, coincided with a
141 significant decline in mean atmospheric $\text{pCO}_2^{\text{atm}}$ at 2.7-2.9 Ma of $\sim 40-90 \mu\text{atm}$ ($\text{mean}_{3.0-3.2\text{Ma}} -$
142 $\text{mean}_{2.4-2.7\text{Ma}} = 66 \pm 26 \mu\text{atm}$; $p < 0.001$ (two-tailed), $n=40$).

143

144 **Efficiency of climate feedbacks**

145 The high fidelity of the boron isotope $\text{pH}/\text{pCO}_2^{\text{atm}}$ proxy (Extended Data Figure 2), coupled with the
146 high resolution of our new $\text{pCO}_2^{\text{atm}}$ record, offers an opportunity to examine the sensitivity of Earth's
147 climate system to forcing by CO_2 during a period when Earth's climate was, on average, warmer than

148 today⁴⁰. For this exercise, global temperature estimates are also needed. We consider two
149 approaches for this. The first is an estimate of global mean annual surface air temperature change
150 (Δ MAT) over the last 3.5 million years, from a scaling of the northern hemisphere climate required
151 to drive an ice-sheet model to produce deep ocean temperature and ice-volume changes consistent
152 with benthic $\delta^{18}\text{O}$ data (Fig 3a,b)³⁵. This approach produces a continuous record of global
153 temperature that agrees well with independent constraints for discrete time intervals (see ref. 35).

154 We supplement Δ MAT with a record from a second approach, which is independent from benthic
155 $\delta^{18}\text{O}$ values. For this, we generated a sea surface temperature stack (SSTst) from 0 to 3.5 Myr ago
156 (Fig. 3c,d), comprising 10 high-resolution (average ~ 4 kyr) SST records based on U^k_{37} alkenone
157 unsaturation ratios, from latitudes between 41°S and 57°N . The selected sites (see Extended Data
158 Figure 1b) all offer near-continuous temporal coverage of the last 3.5 Myr (see Methods). Our SSTst
159 record agrees well with independent, higher density compilations of global SST change^{32,41} (Fig 3c
160 blue line), indicating that SSTst offers a reliable approximation of global SST change (see Methods for
161 more details). Moreover, our SSTst allows us to directly compare the major SST changes, within the
162 same archives, between the Plio-Pleistocene and late Pleistocene.

163 When comparing temperature records from the two approaches considered, it must be emphasized
164 that Δ MAT reflects global mean annual surface air temperature change, while SSTst approximates
165 global mean sea surface temperature change. Hence, their amplitudes of variability will be different,
166 mainly because SSTst does not include temperature changes over land. Approximately, $\Delta\text{SST} = \Delta\text{MAT}$
167 * 0.66 (ref. 32,42), but direct conversion is not needed here, as we merely aim to contrast Pliocene
168 climate behaviour with that for the Pleistocene, within the same data types.

169 To determine the sensitivity of global SST and Δ MAT to CO_2 forcing in the Pliocene and Pleistocene,
170 we use time series of forcing calculated from our new and existing CO_2 records (Fig 3e to h), and
171 regress these against both Δ MAT and SSTst (Fig 3a to d; Supplementary Information Tables 1-3). The
172 regression slopes then describe the average temperature change (ΔT in K) per W per m^2 of forcing

173 (ΔF) for each time interval. These gradients therefore approximate the commonly used sensitivity
174 parameter ($S = \Delta T / \Delta F \text{ K W}^{-1} \text{ m}^2$) for describing global temperature change for a given forcing³. In this
175 scheme, a doubling of atmospheric CO_2 is equivalent to a forcing of 3.7 W m^{-2} , so that for the 66%
176 confidence interval of modern climate sensitivity quoted by ref. 1, the present-day equilibrium value
177 of S (S^a , after ref. 3) is $1.5/3.7$ to $4.5/3.7 = 0.4$ to $1.2 \text{ K W}^{-1} \text{ m}^2$. However, using palaeoclimate data it
178 is not possible to determine the direct equivalent of S^a ; instead, such studies constrain a 'past'
179 parameter (S^p), which includes the combined action of both fast and slow feedbacks³. Note that
180 Earth System Sensitivity, ESS (in K) = $S^p \times 3.7$. Explicit accounting for slow feedback processes in
181 determinations of S^p can make it approximate S^a (ref. 3). Following ref. 3, an S^p estimate after
182 accounting for carbon-cycle feedback is indicated by S_{CO_2} , and one accounting for both carbon-cycle
183 and land-ice-albedo feedbacks is $S_{\text{CO}_2, \text{LI}}$, where the latter gives a useful approximation of S^a . We
184 follow this approach, using $S^p = \Delta \text{MAT} / \Delta F$ and $S^{p, \text{SST}} = \Delta \text{SST} / \Delta F$, both in $\text{K W}^{-1} \text{ m}^2$. Note that our
185 determinations of the sensitivity parameter are based on our entire reconstructed time series,
186 rather than on a simple comparison between a limited Pliocene average and the modern average, as
187 was done in previous studies^{3,16}. Since we calculate a S^p (and $S^{p, \text{SST}}$) for the Pliocene and compare this
188 to the late Pleistocene S^p (and $S^{p, \text{SST}}$), we also avoid complications due to independent changes in
189 boundary conditions (such as topographic changes)³⁹ because we assess sensitivity within each
190 relatively short time window (2.3 to 3.3 Ma vs. 0 to 0.8 Ma). In addition, our approach emphasizes
191 relative changes in CO_2 levels and temperature over the intervals considered, rather than absolute
192 values. This improves accuracy because relative changes are much better constrained than absolute
193 temperature and $\text{pCO}_2^{\text{atm}}$ values from proxy data (see Methods for further discussion).

194 Preliminary regression of ΔMAT against Pliocene $\text{pCO}_2^{\text{atm}}$ identified one data point (at 2362 kyr;
195 white circle in Fig. 1d & 2) with a particularly large residual and significant leverage on the least
196 squares regression (a high Cook's distance). With interglacial-like $\text{pCO}_2^{\text{atm}}$ values but glacial-like $\delta^{18}\text{O}$
197 values (Fig 2), this point may reflect a chronological error, or a short period of unusually high air:sea

198 disequilibrium with respect to CO₂ at ODP Site 999. To avoid the influence of this one point on
199 subsequent linear regressions, we have removed it from our $\delta^{11}\text{B-pCO}_2^{\text{atm}}$ record. The remaining
200 pCO₂^{atm} data (73 points) were interpolated to a constant resolution (1 kyr), smoothed with a 20 kyr
201 moving average to reduce short-term noise and resampled back to the original data spacing (~1
202 sample every 13 kyr). A Monte Carlo approach was followed to determine uncertainties for this
203 smoothed record given the uncertainty in the $\delta^{11}\text{B}$ -derived pCO₂^{atm}. Radiative forcing changes due to
204 pCO₂^{atm} changes are calculated using $\Delta F_{\text{CO}_2} = 5.35 \cdot \ln(\text{CO}_2/\text{C}_0) \text{ W m}^{-2}$; where $\text{C}_0 = 278 \mu\text{atm}$ (Fig 3)⁴³.
205 We ignore mean annual forcing by orbital variations because it is small (<0.5 W m⁻² with a periodicity
206 of 100 to 400 kyr)^{31,32} and averages out over the length of our records. Linear regressions of ΔMAT
207 and SSTst *versus* ΔF_{CO_2} were performed using an approach that yields a probabilistic estimate of
208 slope, and hence sensitivity to CO₂ forcing ($S_{\text{CO}_2} = \Delta T/\Delta F_{\text{CO}_2}$ or $S_{\text{CO}_2,\text{LI}} = \Delta T/\Delta F_{\text{CO}_2,\text{LI}}$), which fully
209 accounts for uncertainties in both X and Y variables (see Methods; Fig 4). Fig 5a-d displays
210 probability distribution functions (pdfs) of the determinations of slope for each time interval. This
211 analysis reveals that, irrespective of the global temperature record used (ΔMAT or SSTst), the
212 average global sensitivity of Earth's climate to forcing by CO₂ only (S_{CO_2}) is approximately 2x higher
213 for the Pleistocene than it is for the Pliocene (Fig 4&5). This validates previous inferences of a strong
214 additional feedback factor during the Pleistocene (at pCO₂^{atm} levels below ~280 μatm), which likely
215 arises from the growth and retreat of large northern hemisphere ice sheets and their role in
216 changing global albedo^{31,32}.

217 Given that, to a first order, the Earth system responds to radiative forcing in a consistent fashion,
218 largely independent of the nature of that forcing⁸, we can determine the climate forcing arising from
219 continental ice albedo changes via a relatively simple parameterisation of sea-level change ($\Delta F_{\text{LI}} =$
220 sea-level change (m) $\times 0.0308 \text{ W m}^{-2}$; following ref. 31,32). Several reconstructions of sea-level
221 change partially or completely span the last 3.5 Ma (e.g., ref. 13, 35, 44, 45, and 46 recalculated by
222 12), and we explore the implications of each of these independent records. Cross-plots of combined

223 CO₂ and ice-albedo forcing ($\Delta F_{\text{CO}_2} + \Delta F_{\text{LI}} = \Delta F_{\text{CO}_2, \text{LI}}$) versus ΔMAT and ΔSSTst are shown in Fig 4 for the
224 Pliocene and Pleistocene. Fig 5e-h displays the influence of choices of temperature and sea-level
225 record on our determinations of $S_{\text{CO}_2, \text{LI}}$ ($= \Delta T / \Delta F_{\text{CO}_2, \text{LI}}$). In contrast to S_{CO_2} , $S_{\text{CO}_2, \text{LI}}$ is similar for both the
226 Pliocene and Pleistocene, regardless of temperature record or other parameter choices (Fig 5). This
227 robustly indicates that the apparent difference between Pliocene and Pleistocene climate sensitivity
228 arises almost entirely from ice-albedo feedback influences. It also implies that all of the other
229 feedbacks that amplify climate forcing by CO₂ (e.g. sea-ice and cloud albedo, water vapour,
230 vegetation, aerosols, other GHGs) must have operated with rather similar efficiencies during both
231 the Pliocene and Pleistocene. Thus, we find no evidence that additional (unexpected) positive
232 feedbacks had become active to amplify Earth system sensitivity to CO₂ forcing during the warm
233 Pliocene. Alternatively, if additional positive feedbacks did become active (e.g. increase in steady-
234 state methane concentration or changes in cloud properties), then their effect must have been
235 negated by the loss of other amplifying feedbacks (e.g. Arctic sea-ice) or the addition of more
236 negative feedbacks. This finding is at odds with previous studies (e.g. ref. 16,47) most likely because
237 of differences in our approach to determine Pliocene climate sensitivity (i.e. we determine a *within*-
238 Pliocene sensitivity) and shortcomings in the proxy systems used by the earlier investigations, both
239 in terms of CO₂ and temperatures (e.g. see ref. 48). For instance, Fig 1d (and Extended Data Figure
240 2) indicate that both orbital-scale variability in pCO₂^{atm} and the major decline at 2.7-2.9 Ma are
241 absent from the previously used¹⁶ alkenone-based pCO₂^{atm} records and as a result regressions of
242 temperature and alkenone-derived forcing are poorly defined (Extended Data Figure 2d-f).

243

244 **Constraints on Climate Sensitivity**

245 Using the geological record to directly estimate ECS (and thus S^g) is problematic because information
246 on the appropriate magnitude of a number of key feedbacks (such as vegetation-albedo) is typically
247 unavailable³. Nonetheless, considerable effort has determined that ECS estimates based on the last

248 glacial maximum fall within the range of ECS estimates from other approaches (1.5 to 4.5 K per CO₂
249 doubling, or 0.4 to 1.2 K W⁻¹ m²; ref. 1). Our analysis implies that a similar ECS applies to the Pliocene
250 and early Pleistocene (2.3 to 3.3 Ma; Fig 5; Supplementary Information Table 4). In addition, our
251 estimate of Pliocene S_{CO₂} using ΔMAT lies within a range of 0.6 to 1.5 K W⁻¹ m² (at 95% confidence),
252 meaning that, once all feedbacks have played out for future CO₂ doubling, ESS (= S_{CO₂} x 3.7) will very
253 likely (95% confidence) be <5.2 K and will likely (68% confidence) fall within a range of 3.0 to 4.4 K
254 (Supplementary Information Table 4).

255 In May 2013, atmospheric CO₂ levels crossed the 400 ppm threshold to values last seen during the
256 Pliocene (Fig. 1c). Given current CO₂ emission rates, global temperatures may reach those typical of
257 the warm periods of the Pliocene by 2050¹. Our findings suggest that, if the Earth system behaves in
258 a similar fashion to how it did during the Pliocene as it continues to warm in the coming years, an
259 ECS of 1.5 to 4.5 K per CO₂ doubling¹ likely provides a reliable description of the Earth's temperature
260 response to climate forcing, at least for global temperature rise up to 3 K above the pre-industrial
261 level. Studies of even warmer intervals in the deeper geological past (well before 3.3 Myr ago) are
262 needed to determine whether any additional climate feedbacks should be expected as the Earth
263 warms even further into the 22nd Century if CO₂ emissions continue unabated.

264

265 **References**

266 1 IPCC, 2013: Climate Change 2013: The Physical Science Basis. Contribution of Working Group
267 I to the Fifth Assessment Report of the Intergovernmental Panel on Climate Change [Stocker, T.F., D.
268 Qin, G.-K. Plattner, M. Tignor, S.K. Allen, J. Boschung, A. Nauels, Y. Xia, V. Bex and P.M. Midgley
269 (eds.)]. Cambridge University Press, Cambridge, United Kingdom and New York, NY, USA, 1535 pp
270 (2013).

271 2 Arrhenius, S. On the influence of carbonic acid in the air upon the temperature of the
272 ground. *Philosophical Magazine and Journal of Science* 5, 237-276 (1896).

273 3 Rohling, E. J. *et al.* Making sense of palaeoclimate sensitivity. *Nature* **491**, 683-691,
274 doi:10.1038/nature11574 (2012).

275 4 Crucifix, M. Does the Last Glacial Maximum constrain climate sensitivity? *Geophys. Res. Lett.*
276 33, doi:10.1029/2006GL027137, 022006 (2006).

277 5 Caballero, R. & Huber, M. State-dependent climate sensitivity in past warm climates and its
278 implication for future climate projections. *PNAS*, 110 (35), 14162-
279 14167doi:www.pnas.org/cgi/doi/10.1073/pnas.1303365110 (2013).

280 6 Beerling, D. J., Fox, A., Stevenson, D. S. & Valdes, P. J. Enhanced chemistry-climate feedbacks
281 in past greenhouse worlds. *PNAS* 108, 9770-9775, doi: 10.1073/pnas.1102409108 (2011).

282 7 Meraner, K., Mauritsen, T. & Voigt, A. Robust increase in equilibrium climate sensitivity
283 under global warming. *Geophys. Res. Lett.* 40, 5944-5948, doi:10.1002/2013GL058118 (2013).

284 8 Hansen, J. *et al.* Efficacy of climate forcings. *J. Geophys. Res.* 110,
285 doi:10.1029/2005JD005776 (2005).

286 9 Byrne, B. & Goldblatt, C. Radiative forcing at high concentrations of well-mixed greenhouse
287 gases. *Geophys. Res. Lett.* 41, 152-160, doi:10.1002/2013GL058456. (2013).

288 10 Lunt, D. J. *et al.* Earth system sensitivity inferred from Pliocene modelling and data. *Nature*
289 *Geoscience* 3, 60-64, doi:10.1038/NGEO706 (2010).

290 11 Haywood, A. M. & Valdes, P. J. Modelling Pliocene warmth: contribution of atmosphere,
291 oceans and cryosphere. *Earth Planet. Sci. Lett.* 218, 363-377 (2004).

292 12 Miller, K. G. *et al.* High tide of the warm Pliocene: Implications of global sea level for
293 Antarctic deglaciation. *Geology* 40, 407-410, doi:10.1130/G32869.1 (2012).

294 13 Rohling, E. J. *et al.* Sea-level and deep-sea-temperature variability over the past 5.3 million
295 years. *Nature* 508, 477-482, doi:10.1038/nature13230 (2014).

296 14 Lunt, D. J. *et al.* On the causes of mid-Pliocene warmth and polar amplification. *Earth Planet.*
297 *Sci. Lett.* 321-322, 128-138, doi:10.1016/j.epsl.2011.12.042 (2012).

298 15 Haywood, A. M. et al. Large-scale features of Pliocene climate: results from the Pliocene
299 Model Intercomparison Project. *Clim. Past* 9, 191-209, doi:10.5194/cp-9-191-2013 (2013).

300 16 Pagani, M., Liu, Z., LaRiviere, J. & Ravelo, A. C. High Earth-system climate sensitivity
301 determined from Pliocene carbon dioxide concentrations. *Nature Geoscience* 3, 27-30, doi:DOI:
302 10.1038/NGEO724 (2010).

303 17 Beerling, D. J. & Royer, D. L. Convergent Cenozoic CO₂ history. *Nature Geoscience* 4, 418-420,
304 doi:10.1038/ngeo1186 (2011).

305 18 Henehan, M. J. et al. Calibration of the boron isotope proxy in the planktonic foraminifera
306 *Globigerinoides ruber* for use in palaeo-CO₂ reconstruction. *Earth Planet. Sci. Lett.* 364, 111-122,
307 doi:10.1016/j.epsl.2012.12.029 (2013).

308 19 Hönisch, B. & Hemming, N. G. Surface ocean pH response to variations in pCO₂ through two
309 full glacial cycles. *Earth Planet. Sci. Lett.* 236, 305-314 (2005).

310 20 Foster, G. L. Seawater pH, pCO₂ and [CO₃²⁻] variations in the Caribbean Sea over the last 130
311 kyr: A boron isotope and B/Ca study of planktic foraminifera. *Earth Planet. Sci. Lett.* 271, 254-266
312 (2008).

313 21 Takahashi, K. et al. Climatological mean and decadal change in surface ocean pCO₂, and net
314 sea-air CO₂ flux over the global oceans. *Deep-Sea Res. II* 56, 554-577 (2009).

315 22 Lisiecki, L. E. & Raymo, M. E. A Pliocene-Pleistocene stack of 57 globally distributed benthic
316 δ¹⁸O records. *Paleoceanography* 20, doi: 10.1029/2004PA001071 (2005).

317 23 Bartoli, G., Hönisch, B. & Zeebe, R. Atmospheric CO₂ decline during the Pliocene
318 intensification of Northern Hemisphere Glaciations. *Paleoceanography* 26, PA4213,
319 doi:4210.1029/2010PA002055 (2012).

320 24 Davis, C.V., Badger, M.P.S., Bown, P.R. & Schmidt, D.N. The response of calcifying plankton
321 to climate change in the Pliocene, *Biogeosciences*, 10, 6131-6139 (2013).

322 25 Seki, O. et al. Alkenone and boron based Plio-Pleistocene pCO₂ records. *Earth Planet. Sci.*
323 *Lett.* 292, 201-211 (2010).

324 26 Badger, M. P. S., Schmidt, D. N., Mackensen, A. & Pancost, R. D. High resolution alkenone
325 palaeobarometry indicates relatively stable pCO₂ during the Pliocene (3.3 to 2.8 Ma). *Philos. Trans.*
326 *Royal Soc. A* 347, 20130094, doi: 10.1098/rsta.2013.0094 (2013).

327 27 Petit, J. R. et al. Climate and atmospheric history of the past 420,000 years from the Vostok
328 ice core, Antarctica. *Nature* 399, 429-436 (1999).

329 28 Lüthi, D. et al. High-resolution carbon dioxide concentration record 650,000-800,000 years
330 before present. *Nature* 453, 379-382, doi:10.1038/nature06949 (2008).

331 29 Siegenthaler, U. et al. Stable carbon cycle-climate relationship during the Late Pleistocene.
332 *Science* 310, 1313-1317 (2005).

333 30 Hönisch, B., Hemming, G., Archer, D., Siddal, M. & McManus, J. Atmospheric carbon dioxide
334 concentration across the Mid-Pleistocene Transition. *Science* 324, 1551-1554 (2009).

335 31 Köhler, P. et al. What caused Earth's temperature variations during the last 800,000 years?
336 Data-based evidence on radiative forcing and constraints on climate sensitivity. *Quat. Sci. Reviews*
337 29, 129-145, doi:10.1016/j.quascirev.2009.09.026 (2010).

338 32 Rohling, E. J., Medina-Elizalde, M., Shepherd, J. G., Siddall, M. & Stanford, J. D. Sea surface
339 and High-latitude temperature sensitivity to radiative forcing of climate over several glacial cycles.
340 *J. Climate* 25, 1635-1656, doi:10.1175/2011JCLI4078.1 (2012).

341 33 DeConto, R. M. et al. Thresholds for Cenozoic bipolar glaciation. *Nature* 455, 652-656 (2008).

342 34 Shackleton, N. Oxygen isotope analyses and Pleistocene temperatures re-assessed. *Nature*
343 215, 15-17 (1967).

344 35 van de Wal, R. S. W., de Boer, B., Lourens, L. J., Köhler, P. & Bintanja, R. Reconstruction of a
345 continuous high-resolution CO₂ record over the past 20 million years *Clim. Past* 7, 1459-1469,
346 doi:10.5194/cp-7-1459-2011 (2011).

347 36 Balco, G. & Rovey, C. W., II. Absolute chronology for major Pleistocene advances of the
348 Laurentide Ice Sheet. *Geology* 38, 795-798, doi:10.1130/G30946.1 (2010).

349 37 Bailey, I. et al. An alternative suggestion for the Pliocene onset of major northern
350 hemisphere glaciation based on geochemical provenance of North Atlantic Ocean ice-rafted debris.
351 *Quat. Sci. Reviews* 75, 181-194, doi:10.1016/j.quascirev.2013.06.004 (2013).

352 38 Hidy, A. J., Gosse, J. C., Froese, D. G., Bond, J. D. & Rood, D. H. A latest Pliocene age for the
353 earliest and most extensive Cordilleran Ice Sheet in northwestern Canada. *Quat. Sci. Reviews* 61, 77-
354 84, doi:10.1016/j.quascirev.2012.11.009 (2013).

355 39 Lunt, D. J., Foster, G. L., Haywood, A. M. & Stone, E. J. Late Pliocene Greenland glaciation
356 controlled by a decline in atmospheric CO₂ levels. *Nature* 454, 1102-1105 (2008).

357 40 Dowsett, H. J. et al. Assessing confidence in Pliocene sea surface temperatures to evaluate
358 predictive models. *Nature Climate Change* 2, 365-371, doi:10.1038/NCLIMATE1455 (2012).

359 41 Shakun, J. D. et al. Global warming preceded by increasing carbon dioxide concentrations
360 during the last deglaciation. *Nature* 484, 49-54, doi:10.1038/nature10915 (2012).

361 42 Williams, R. G., Goodwin, P., Ridgwell, A. & Woodworth, P. L. How warming and steric sea
362 level rise relate to cumulative carbon emissions. *Geophys. Res. Lett.* 39, doi: 10.1029/2012GL052771
363 (2012).

364 43 Myhre, G., Highwood, E. J., Shine, K. P. & Stordal, F. New estimates of radiative forcing due
365 to well mixed greenhouse gases. *Geophys. Res. Lett.* 25, 2715-2718 (1998).

366 44 Rohling, E. J. et al. Antarctic temperature and global sea level closely coupled over the past
367 five glacial cycles. *Nature Geoscience* 2, 500-504, doi:10.1038/ngeo557 (2009).

368 45 Elderfield, H. et al. Evolution of ocean temperature and ice volume through the Mid-
369 Pleistocene climate transition. *Science* 337, 704-709, doi:10.1126/science.1221294 (2012).

370 46 Naish, T. R. & Wilson, G. S. Constraints on the amplitude of Mid-Pliocene (3.6-2.4 Ma)
371 eustatic sea-level fluctuations from the New Zealand shallow-marine sediment record. *Philos. Trans.*
372 *Royal Soc. A* 367, 169-187, doi: 10.1098/rsta.2008.0223 (2009).

373 47 Federov, A. V. et al. Patterns and mechanisms of early Pliocene warmth. *Nature* 496, 43-49,
374 doi:10.1038/nature12003 (2013).

375 48 O'Brien, C.L. et al., 2014. High sea surface temperatures in tropical warm pools during the
376 Pliocene. *Nature Geoscience* 7, 606-611, doi: 10.1038/ngeo2194.

377 49 Zhang, Y. G., Pagani, M., Liu, Z., Bohaty, S. M. & DeConto, R. M. A 40-million-year history of
378 atmospheric CO₂. *Philos. Trans. Royal Soc. A* 371, 20130096 (2013).

379 50 Kürschner, W. M., van der Burgh, J., Visscher, H. & Dilcher, D. L. Oak leaves as biosensors of
380 late Neogene and early Pleistocene paleoatmospheric CO₂ concentrations. *Mar. Micropal.* 27, 299-
381 312 (1996).

382

383 **Supplementary Information** is linked to the online version of the paper at www.nature.com/nature

384 **Acknowledgements** This study used samples provided by the International Ocean Discovery
385 Program (IODP). We thank Andy Milton at the University of Southampton for maintaining the mass
386 spectrometers used in this study. Soraya Cherry and Thorsten Garlich are acknowledged for their
387 help with sample preparation and Diederik Liebrand is thanked for his assistance with time series
388 analysis. This study was funded by NERC grants NE/H006273/1 to RDP, GLF, DJL and DNS (which
389 supported MAMB and MPSB) and NE/I006346/1 to PFS and GLF. MAMB was also supported by the
390 European Community through a Marie Curie Fellowship and EJR was supported by 2012 Australian
391 Laureate Fellowship FL120100050. GLF also wishes to acknowledge the support of Yale University
392 (as Visiting Flint Lecturer).

393 **Author Contributions** MAMB and TBC collected the data and all relevant calculations were
394 performed by GLF. GLF, MAMB and TBC constructed the first draft of the manuscript and all authors
395 contributed specialist insights that helped refine the manuscript. PFS aided sample preparation for
396 $\delta^{11}\text{B}$ analysis and refined the age models used for ODP Sites 999 and ODP 662 and GLF, RDP, DJL and
397 DNS conceived the study. MAMB and GLF contributed equally to this work.

398 **Author Information** Reprints and permissions information is available at www.nature.com/reprints.

399 The authors declare no competing financial interests. Readers are welcome to comment on the

400 online version of the paper. Correspondence and requests for materials should be addressed to GLF
401 (gavin.foster@noc.soton.ac.uk).

402

403 **Figure Legends**

404 **Figure 1. Records of late Pliocene/early Pleistocene pCO₂^{atm}.** (a) pCO₂^{atm} based on δ¹³C of
405 sedimentary alkenones (dark green circles (ODP 999)²⁵; aquamarine squares (ODP 999)²⁶; dark
406 orange (ODP 1208)¹⁶, purple circles (ODP 806)¹⁶; dark red squares (ODP 925)⁴⁹). Error bars are
407 uncertainty in pCO₂^{atm} at the 95% level of confidence. (b) δ¹¹B of planktic foraminifera from ODP 999
408 (blue closed circles for *G. sacculifer* and squares²⁵ for *G. ruber*²⁵; red squares for *G. sacculifer*²³) and
409 stomatal density of fossil leaves (purple filled circle)⁵⁰. Error bars are uncertainty in pCO₂^{atm} at the
410 95% level of confidence. (c) New boron isotope data from ODP 999 (blue circles) and ODP 662 (red
411 circles). Error bands for ODP 999 denote 1sd (dark blue) and 2sd (light blue) analytical uncertainty,
412 error bars for ODP 662 show 2sd analytical uncertainty. (d) Atmospheric pCO₂ (µatm) determined
413 from data shown in (c) for ODP 999 (blue circles) and ODP 662 (red circles). Error band encompasses
414 68% (dark blue) and 95% (light blue) of 10,000 Monte Carlo simulations of pCO₂^{atm} using the data in
415 (c) and a full propagation of all the key uncertainties (see Methods). For ODP 662 error bars
416 encompass 95% of 10,000 simulations. Dotted lines show the modelled threshold of northern
417 hemisphere glaciation (280 µatm)³³. (e) Benthic δ¹⁸O stack²², prominent marine isotope stages are
418 labelled (blue for glacial, red for interglacial stages). Thick lines on several panels are non-parametric
419 smoothers through the data. Blue open circle on (d) highlights the data point that is identified as
420 outlier in Fig 2 and not used in subsequent regressions.

421 **Figure 2. Relationship between δ¹¹B, climate forcing from CO₂ and δ¹⁸O.** (a) δ¹¹B vs. δ¹⁸O and (b)
422 ln(CO₂/C_o) vs. δ¹⁸O for data from the last 3 million years. Ln(CO₂/C_o) is defined in the text. Boron data
423 in (a) are from this (blue open and closed circles) and published studies (green circles³⁰; blue

424 triangles²⁰). Ice-core CO₂ data shown as open red circles²⁷⁻²⁹. The vertical dashed line is at a CO₂ of
425 278 μatm . The data point removed from subsequent regression analysis is highlighted as open blue
426 circles. Note that the $\delta^{11}\text{B-pCO}_2$ data from ref. 23 are not plotted for clarity. The black line is a non-
427 parametric regression through all the data shown. The $\delta^{11}\text{B}$ data from ref. 30 have been corrected
428 for laboratory and inter-species differences through a comparison between core-top $\delta^{11}\text{B}$ values.

429 **Figure 3. Pleistocene and late Pliocene time series.** (a) and (b) mean annual surface air temperature
430 change (ΔMAT)³⁵, (c) and (d) sea surface temperature change (ΔSST ; this study in red and from a
431 stack of a more comprehensive compilation³² in blue). Uncertainty envelopes at 95% confidence for
432 both temperature records are shown in red. (e) ΔF_{CO_2} for the Pleistocene from ice-core data²⁷⁻²⁹.
433 (f) ΔF_{CO_2} for the late Pliocene calculated using the CO₂ data from this study. (g) $\Delta F_{\text{CO}_2,\text{LI}}$ calculated
434 using data in (e) and published sea-level records (R14¹³, VDW11³⁵ and from ref. 44 for 0-520 kyr and
435 ref. 45 for 520 to 800 kyr, R09+E12). (h) $\Delta F_{\text{CO}_2,\text{LI}}$ for the late Pliocene calculated using the CO₂ data
436 from this study and published sea-level records (ref. 46 recalculated by ref. 12, N09, R14¹³,
437 VDW11³⁵). Error bands in (e) to (h) represent the uncertainty in smoothed CO₂ record and sea-level
438 (68% and 95% confidence in light and dark respectively) propagated using a Monte Carlo approach
439 ($n=1000$) for each reconstruction.

440 **Figure 4. Cross plots of forcing and temperature response.** (a) ΔMAT vs. ΔF_{CO_2} and (b) to (d) ΔMAT
441 vs. $\Delta F_{\text{CO}_2,\text{LI}}$ for the following sea-level records detailed in the caption for Figure 3: (b) R09+E12^{44,45} and
442 N09^{12,46} (c) VDW11³⁵, (d) R14¹³. (e) ΔSST vs. ΔF_{CO_2} and (f) to (h) ΔSST vs. $\Delta F_{\text{CO}_2,\text{LI}}$ for the same sea-
443 level records as in panels (b) to (d). In all panels late Pleistocene data (0-800 kyr) are shown as red
444 open circles and late Plio-Pleistocene (2300-3300 kyr) as blue open circles. Regression lines fitted by
445 least-squares regression are also shown in the appropriate colour (shaded bands represent 95%
446 confidence intervals). For (a) to (d) the temperature record is that of ref. 35 and for (e) to (h) it is
447 SSTst from this study. In all cases the slope (m) and standard error uncertainty are determined by
448 least squares regression. Also shown are the p values for the regressions.

449 **Figure 5. Probability density functions of the slope from regressions of temperature against**
450 **climate forcing.** (a,c,e,g) ΔMAT and (b,d,f,h) ΔSST against ΔF_{CO_2} and $\Delta F_{\text{CO}_2, \text{LI}}$ for the Pleistocene (a, b,
451 e, f) and Pliocene (c, d, g, h), taking into account the uncertainties on all variables (see text). In (e) to
452 (h) individual pdfs are shown for different choices of sea-level, the combined pdf shown in bold is
453 the sum of these different pdfs and therefore also incorporates uncertainty related to the choice of
454 sea-level record. Also shown and labelled are the median (bold), 68th percentile (dot-dash) and 95th
455 percentiles (dotted).

456

457 **Methods**

458 **Sample locations.** We present new data from two deep ocean sites: ODP Site 999 (Caribbean Sea,
459 12°44.64'N and 78°44.36'W) and ODP Site 662 (Equatorial Atlantic, 1°23.41'S, 11°44.35'W). Both
460 sites have well-constrained age models for the Pliocene and are part of the Lisiecki and Raymo
461 benthic foraminifera $\delta^{18}\text{O}$ stack²² (hereafter LR04). Sedimentation rates are comparable between the
462 sites (~3 cm/kyr at ODP 999 and ~4 cm/kyr at ODP 662). At ODP Site 999, seventy four samples were
463 analysed at an average temporal resolution of around 1 sample every 13 kyr, targeting several glacial
464 and interglacial maxima. ODP Site 662 was analysed at much lower resolution (8 samples in 1000 kyr
465 = 1 sample every 125 kyr on average), and the chosen samples were limited to peak interglacial
466 conditions to avoid potential upwelling influences during glacial periods⁵¹. The extent of the modern
467 air-sea CO_2 disequilibrium at each location is displayed in Extended Data Fig 1a.

468 **Analytical methodology.** Between 90 and 200 individuals of *Globigerinoides ruber* (~10 $\mu\text{g}/\text{shell}$)
469 were picked from the 300-355 μm size fraction from ODP Sites 999 and 662. Foraminiferal samples
470 were crushed between cleaned glass microscope slides and subsequently cleaned according to
471 established oxidative cleaning methods⁵²⁻⁵⁴. After cleaning, samples were dissolved in ~0.15 M
472 Teflon-distilled HNO_3 , centrifuged and transferred to 5 ml Teflon vials for storage. An aliquot (~20 μl ;

473 ~7% of the total sample) was taken for trace element analysis. Boron was separated from the
 474 dissolved samples using Amberlite IRA-743 boron-specific anion exchange resin following established
 475 procedures²⁰. Boron isotope ratios were measured on a Thermo Scientific Neptune multicollector
 476 inductively coupled plasma mass spectrometer (MC-ICPMS) at the University of Southampton
 477 according to methods described elsewhere^{18,20,54}.

478 External reproducibility of $\delta^{11}\text{B}$ analyses is calculated following the approach of ref. 54, and is
 479 described by the relationship:

$$480 \quad 2\sigma = 1.87 \cdot \exp^{-20.6[^{11}\text{B}]} + 0.22 \cdot \exp^{-0.43[^{11}\text{B}]} \quad [1]$$

481 where [^{11}B] is the intensity of the ^{11}B signal in volts (see ref. 18 for further details).

482 Trace elements were measured on a Thermo Scientific Element 2 single collector ICPMS at the
 483 University of Southampton, following established methods²⁰. Over the period 2012-2013, analytical
 484 reproducibility for Mg/Ca was $\pm 2.7\%$ (2σ). Raw Mg/Ca ratios were corrected for changes in the
 485 Mg/Ca ratio of seawater ($\text{Mg}/\text{Ca}_{\text{sw}}$) using the approach of ref. 55 using the power-law modification
 486 of ref. 56 and the modelled $\text{Mg}/\text{Ca}_{\text{sw}}$ of ref. 57. Specifically, we use a H value⁵⁶ of 0.41, originally
 487 derived for *Globigerinoides sacculifer*⁵⁸, as no species-specific H value is currently available for *G.*
 488 *ruber* (for extended discussion, see ref. 48). The following equation^{56,59} was therefore used to derive
 489 calcification temperatures from our Mg/Ca ratios, which also includes a depth correction to account
 490 for the influence of dissolution on shell Mg/Ca ratios.

$$491 \quad T(^{\circ}\text{C}) = \frac{\ln\left(\frac{\text{Mg}}{\text{Ca}_{\text{test}}}\right) / \left(E \times \left(\frac{\text{Mg}}{\text{Ca}}\right)_{\text{sw}}^t\right)^H}{0.09} + (0.61 \times Z) \quad [2]$$

492 Where $\left(\frac{\text{Mg}}{\text{Ca}}\right)_{\text{sw}}^t$ is the Mg/Ca ratio of seawater at the time of interest, Z is the core depth in km and E
 493 is defined by the following equation⁵⁶:

$$E = \frac{0.38}{\left(\left(\frac{Mg}{Ca}\right)_{sw}^t\right)^H}$$

494 Trace element data were also used to check the efficiency of the foraminiferal cleaning
 495 procedure^{20,54}. All samples had Al/Ca ratios of <100 μmol/mol, and typically <60 μmol/mol.

496 **Determination of pH from δ¹¹B of *G. ruber*.** Boron in seawater exists mainly as two different species,
 497 boric acid (B(OH)₃) and borate ion (B(OH)₄⁻), and their relative abundance is pH dependent. There are
 498 two isotopes of boron, ¹¹B (~80%) and ¹⁰B (~20%), with a ratio normally expressed in delta notation
 499 as:

$$500 \quad \delta^{11}\text{B}(\text{‰}) = \left[\left(\frac{{}^{11}\text{B}/{}^{10}\text{B}_{\text{sample}}}{{}^{11}\text{B}/{}^{10}\text{B}_{\text{NIST951}}} \right) - 1 \right] \times 1000 \quad [3]$$

501 where ¹¹B/¹⁰B_{NIST951} is the isotopic ratio of NIST SRM 951 boric acid standard (¹¹B/¹⁰B = 4.04367; ref.
 502 60).

503 There is a pronounced isotopic fractionation between the two dissolved boron species, with boric
 504 acid being enriched in ¹¹B by 27.2‰ (ref. 61). As the concentration of each species is pH dependent,
 505 their isotopic composition also has to change with pH in order to maintain a constant seawater δ¹¹B.
 506 Calibration studies^{54,62,63} have shown that the borate species is predominantly incorporated into
 507 foraminiferal CaCO₃, and therefore ocean pH can be calculated from the δ¹¹B of borate (δ¹¹B_{borate}) as
 508 follows:

$$509 \quad \text{pH} = \text{pK}_B^* - \log \frac{\frac{\delta^{11}\text{B}_{\text{sw}} - \delta^{11}\text{B}_{\text{borate}}}{\delta^{11}\text{B}_{\text{sw}} - ({}^{11-10}\text{K}_B \cdot \delta^{11}\text{B}_{\text{borate}}) - 1000 \cdot ({}^{11-10}\text{K}_B - 1)}}{\delta^{11}\text{B}_{\text{sw}} - ({}^{11-10}\text{K}_B \cdot \delta^{11}\text{B}_{\text{borate}}) - 1000 \cdot ({}^{11-10}\text{K}_B - 1)}} \quad [4]$$

510 where pK_B^{*} is the dissociation constant for boric acid at in situ temperature, salinity and pressure⁶⁴,
 511 δ¹¹B_{sw} is the isotopic composition of seawater (39.61‰; ref. 65), δ¹¹B_{borate} is the isotopic

512 composition of borate ion, and $^{11-10}K_B$ is the isotopic fractionation between the two aqueous species
513 of boron in seawater (1.0272 ± 0.0006) (ref. 61).

514 In our calculations, temperature for ODP Site 999 is derived from Mg/Ca ratios measured on aliquots
515 (separated after dissolution) of the same samples used for $\delta^{11}B$ analysis and for ODP Site 662 from
516 published records of temperature using the U^{K}_{37} proxy⁶⁶. Despite the uncertainty in Mg/Ca-derived
517 SST's we have not used published U^{K}_{37} temperature records for ODP Site 999 because they are of
518 lower temporal resolution and close to saturation ($T = 28-29$ °C)²⁵. Salinity has little influence on the
519 calculations of pH (± 1 psu = ± 0.006 pH units), and therefore is assumed to be constant at 35 psu
520 (similar to the present-day mean annual average at both locations). The uncertainty associated with
521 this assumption is propagated into pCO_2^{atm} calculations.

522 Boron has a long residence time in seawater (10-20 Ma; ref. 67), and to account for likely (small)
523 changes in the boron isotopic composition of seawater ($\delta^{11}B_{sw}$) over the last 3 million years, we use a
524 simple linear extrapolation between modern $\delta^{11}B_{sw}$ (39.61‰; ref. 65) and the $\delta^{11}B_{sw}$ determined by
525 ref. 68 for the middle Miocene (12.72 Ma; $\delta^{11}B_{sw} = 37.8$ ‰). This simple estimation yields $\delta^{11}B_{sw} =$
526 39.2‰ at 3 Ma, which is consistent with available independent constraints, for example based on
527 assumptions of bottom water pH and measured benthic foraminiferal $\delta^{11}B$ (ref. 69).

528 Finally, in order to calculate pH from the $\delta^{11}B$ of *G. ruber*, it is necessary to account for species-
529 specific differences between $\delta^{11}B_{borate}$ in ambient seawater and $\delta^{11}B$ in foraminiferal calcite
530 ($\delta^{11}B_{calcite}$; i.e., "vital effects"). Here we used the species- and size-specific calibration equation of ref.
531 18 for *G. ruber* 300-355 μm (Equation 5). This equation has been applied in previous studies¹⁸ to
532 produce a $\delta^{11}B$ -based atmospheric pCO_2 (pCO_2^{atm}) record for the last 30 kyr that is in very good
533 agreement with ice-core pCO_2^{atm} records (Extended Data Figure 2).

534
$$\delta^{11}B_{borate} = (\delta^{11}B_{calcite} - 8.87 \pm 1.52) / 0.60 \pm 0.08 \text{ (uncertainty at } 2\sigma)$$
 [5]

535 It is important to note that, not only is there generally good preservation of the sites we use^{23,24}, but
536 also the $\delta^{11}\text{B}$ of *G. ruber* does not appear to be significantly affected by partial dissolution²⁵.

537 **Determination of $\text{pCO}_2^{\text{atm}}$ from $\delta^{11}\text{B}$ -derived pH.** Another variable of the ocean carbonate system is
538 required besides pH in order to calculate the partial pressure of CO_2 in seawater (pCO_2^{sw})⁷⁰. Here,
539 total alkalinity (TA) is assumed to be constant at values similar to modern at ODP Site 999 (2330
540 $\mu\text{mol}/\text{kg}$; ref. 20). It is important to note that pCO_2^{sw} estimates are mostly determined by the
541 reconstructed pH and that TA has little influence. This is because pH reflects the *ratio* of TA to DIC
542 (total dissolved inorganic carbon), so when pH is known the ratio of TA:DIC is set, so the effect on
543 pCO_2^{sw} of a large increase/decrease in TA is partially countered by an opposite change in DIC.
544 Indeed, at a given pH, a change in TA by 10% only results in a pCO_2^{sw} change of 10%. For example,
545 modifying TA by $\pm 100 \mu\text{mol}/\text{kg}$ (a range equivalent to modelled variations in TA for the last 2 million
546 years; ref. 30) only modifies reconstructed pCO_2^{sw} (when pH is known) by less than $\pm 12 \mu\text{atm}$.

547 pCO_2^{sw} was calculated using the equations of ref. 70, the “seacarb” package of R (ref. 71) and a
548 Monte Carlo approach ($n = 10,000$) to fully propagate the uncertainty in the input parameters (at
549 95% confidence or full range, where appropriate): $\delta^{11}\text{B}$ (\pm analytical uncertainty, calculated using
550 Equation [1], and calibration uncertainty in Equation [5]), Mg/Ca-derived temperature ($\pm 3 \text{ }^\circ\text{C}$),
551 salinity ($\pm 3 \text{ psu}$), TA ($\pm 175 \mu\text{mol}/\text{kg}$), $\delta^{11}\text{B}_{\text{sw}}$ ($\pm 0.4\text{‰}$). $\text{pCO}_2^{\text{atm}}$ was then calculated from pCO_2^{sw} using
552 Henry’s Law and subtracting the modern disequilibria with respect to CO_2 at the two sites (Extended
553 Data Figure 1; Supplementary Information Tables 1&2). Note that for the quoted uncertainty range
554 for temperature, salinity, and $\delta^{11}\text{B}_{\text{sw}}$ a normal distribution is assumed. However, for TA we have
555 assumed a “flat” probability (i.e. an equal probability of TA being any value between 2155 and 2505
556 $\mu\text{mol}/\text{kg}$). We therefore do not ascribe weight to the assumption that TA remains constant, but
557 rather fully explore the likely range given the available, model based, constraints^{72,73}. It should also
558 be noted that salinity and temperature have little control on our estimated pCO_2^{sw} ($+1 \text{ psu} = +0.2$
559 μatm ; $+1 \text{ }^\circ\text{C} = +8 \mu\text{atm}$).

560 **Comparison with published records of Pliocene pCO₂^{atm}.** Figure 1 and Extended Data Figures 2b&c
561 show a comparison of our new high resolution $\delta^{11}\text{B}$ -derived pCO₂^{atm} record with published records.
562 As noted in the main text, although the various approaches agree, in detail our new record exhibits
563 more structure. As a consequence, cross plots of the previously published CO₂ data against ΔMAT
564 (or SSTst) are largely incoherent (Extended Data Figure 2d-f). In the case of the stomatal estimates⁵⁰
565 and the existing $\delta^{11}\text{B}$ -based records^{23, 25} this is largely a consequence of their low temporal
566 resolution, although analytical issues⁷⁴ and species choice (we use *G. ruber* that spends its entire life
567 cycle in the mixed layer whereas ref. 23 uses *G. sacculifer* that migrates during its life cycle and
568 whose $\delta^{11}\text{B}$, unlike *G. ruber*, is modified by partial dissolution²⁵) may also play a role for the
569 discrepancy with earlier $\delta^{11}\text{B}$ records (see ref. 25 for further discussion). The lack of variability
570 through the Pliocene for the alkenone-based records may be related to changes in the size of the
571 alkenone producers²⁶, fluctuations in nutrient content/water depth of maximum alkenone
572 production, and/or variations in the degree of passive vs. active uptake of CO₂ by the alkenone
573 producing coccolithophorids^{49,75}.

574 **Continuous records of Pliocene and late Pleistocene global temperature change.** Robust records of
575 global temperature change are needed to determine how the Earth's climate has responded to
576 changes in CO₂. Here we estimate this variable using two independent approaches: (i) we generate a
577 stack of available sea surface temperature records (SSTst); and (ii) following ref. 35 we use a
578 reconstruction of global mean annual surface air temperature change based on a scaling of the
579 northern hemisphere temperature required by a simple coupled ice-sheet-climate model to forward
580 model the benthic $\delta^{18}\text{O}$ stack of ref. 76 (tuned here to the LR04 age model; ΔMAT).

581 For the SST stack (SSTst) we imposed a number of criteria for site selection. These are: (i) the record
582 must be continuous from late Pliocene to late Pleistocene (or nearly so); (ii) the temporal resolution
583 must be relatively high (ideally better than 1 sample per 10 kyr; for ODP Site 1237 we have however
584 accepted a lower resolution to increase spatial coverage) to allow us to fully resolve the dominant

585 orbital-scale variability; (iii) be based on U_{37}^k , given that Mg/Ca suffers an unacceptable level of
586 uncertainty on these timescales due to the secular evolution of the Mg/Ca ratio of seawater (e.g.,
587 ref. 48); and (iv) the temperatures recorded by the U_{37}^k proxy must be less than 29 °C, above which
588 the proxy becomes saturated and therefore unresponsive⁷⁵. Ten published records meet these
589 criteria (ODP Sites 982, 607, 1012, 1082, 1239, 846, 662, 722, 1237 and 1090; ref. 66, 78-85) and the
590 locations of these sites are shown in Extended Data Figure 2b. The average temporal resolution of
591 these records is 1 sample every ~4 kyr (ranging from ~2 to ~13 kyr) and the published age model of
592 each site is either part of the LR04 stack or was tuned to it (see the original publications for details).

593 In order to stack the records, each was first converted to a relative SST record referenced to either
594 the average of the Holocene (0-10 kyr), or mean annual modern SST if the Holocene is missing, and
595 then linearly interpolated to a 5 kyr spacing. These relative records are then averaged to produce a
596 single stacked record of relative SST change (SSTst; Supplementary Information Table 5). The
597 number of sites contributing to SSTst varies but for most of the record is ≥ 8 (Extended Data Figure
598 6a&b). Uncertainty on SSTst is estimated by a Monte Carlo procedure where 1000 realisations are
599 made of each individual SST record with noise added reflecting the magnitude of analytical
600 uncertainty in the U_{37}^k SST reconstruction (± 1 °C at 2σ ; ref. 75). Since we are using the same proxy
601 for each location it is not necessary to consider the calibration uncertainty as this should be the
602 same for each record. Each SST realisation is then averaged to produce 1000 realisations of SSTst.
603 The mean of these 1000 realisations is then calculated and the 95% confidence interval is given by
604 the 2.5% and 97.5% percentile (red band on Figure 3). Jackknifing of SSTst (i.e. the sequential removal
605 of one record at a time) indicates that no particular record has undue influence and SSTst remains
606 close to the bounds relating to analytical uncertainty (the grey lines on Extended Data Figure 6c&d).

607 Our aim with SSTst was not to specifically reconstruct global SST change but rather to examine the
608 change in SST at these locations for a given forcing in the Pliocene and Pleistocene. We therefore do

609 not require SSTst to reflect global SST change. However, in order to assess how well SSTst does
610 reflect global SST we:

611 (i) Examined the mean of historic SST change (1870AD to 2013 AD; from the HadISST
612 database; ref. 86) at each location where we have an alkenone palaeo-SST record. This
613 comparison is shown in Extended Data Figure 7 (blue circles). Despite exhibiting more
614 variability than the mean annual global average (red in Extended Data Figure 7), these
615 10 sites clearly capture the global long term trend in global mean SST^{87,88} over the last
616 140 years or so (Extended Data Figure 7).

617 (ii) Compare SSTst to a multi-proxy and more comprehensive and independent compilation
618 of ref. 32 that covers the last 100 kyr with >30 sites and the last 278 kyr with >10 sites.
619 When data for the last 278 kyr are stacked together in a similar way to SSTst, the stack
620 of ref. 32 (blue on Fig 3c) compares well with SSTst giving us confidence that it closely
621 reflects global SST change.

622 (iii) Compare SSTst to discrete global reconstructions of SST. For the last glacial (20-25 kyr)
623 SSTst gives a Δ SST of -2.2 ± 0.4 K, which is close to the Δ SST of -3.2 K from a recent
624 comprehensive compilation for the LGM⁴² and is within uncertainty of earlier
625 reconstructions (e.g., ref. 85 where Δ SST of -1.9 ± 1.8 K). For the Mid-Pliocene Warm
626 Period (3-3.3 Ma), SSTst gives an average of $+2.3$ K. A simple mean calculated from the
627 larger multi-proxy PRISM SST compilation of ref. 40 is very similar at $+2.6$ K. SSTst is
628 slightly warmer than an area weighted mean of the PRISM SST set ($+2$ K; ref. 40).

629 Taken together, these comparisons clearly indicate that, although SSTst is made of a limited number
630 of sites, it does appear to closely reflect change in global SST. This conclusion is also supported by
631 the general agreement between the trends (but not absolute values) exhibited by Δ MAT and SSTst
632 through the Pliocene and Pleistocene (Fig. 3), with subtle differences between these two climate

633 records (e.g. at 2.8 Ma) potentially a result of a decoupling between deep and surface water
634 temperature evolution, small spatial biases in our SST stack, and/or minor age-model inaccuracies.

635 **Regression-based determinations of climate sensitivity** In order to examine the climatic response
636 (expressed as either ΔMAT or ΔSST) to forcing by CO_2 and land-ice albedo changes in both time
637 periods, we used a linear regression approach. Because each variable used (CO_2 and SL, ΔMAT or
638 ΔSST) has an associated uncertainty, however, it is necessary to fully explore the influence of these
639 uncertainties on our estimates of slope determined using least squares linear regression. Due to
640 difficulty of performing least squares linear regression with uncertainty in X- and Y- variables that are
641 not necessarily normally distributed we have used a two stage approach to fully propagate all the
642 uncertainties involved. Firstly, we generated 1000 realisations of each temporal record of each
643 variable (e.g. ΔF_{CO_2} , $\Delta F_{\text{CO}_2, \text{LI}}$, ΔMAT or ΔSST) based on a random sampling of each record within its
644 uncertainty envelope. This uncertainty envelope was either a simple normal distribution (e.g. ± 6
645 ppm for ice-core CO_2) or based on other Monte Carlo output (e.g. random sampling the 10,000
646 simulations of the Pliocene $\delta^{11}\text{B}$ - $\text{pCO}_2^{\text{atm}}$ record or the 1000 realisations of SSTst; see above). Then
647 the first realisation of the ΔF_{CO_2} (or $\Delta F_{\text{CO}_2, \text{LI}}$) record was regressed against the first realisation of the
648 ΔMAT (or ΔSST) with the uncertainty in the slope and intercept of that regression determined using
649 a bootstrapping approach ($n=1000$; ref. 90). The second realisation of the forcing term and the
650 climate response was then regressed and the 1000 estimates of slope and intercept by
651 bootstrapping were combined with 1000 of the first regression. This continued for all 1000
652 realisations and a probability density function for the slope and intercept, accounting for X- and Y-
653 uncertainty, was then constructed from the combined bootstrap estimates for each realisation
654 ($n=1000000$). The results of this approach are shown in Fig 5.

655 As noted above, $\text{pCO}_2^{\text{atm}}$ (and hence ΔF_{CO_2}) calculated from boron isotopes is a function of not only
656 the measured $\delta^{11}\text{B}$ but also the total alkalinity (TA; or other second carbonate system variable) and,
657 beyond the last 1 million years or so, the boron isotopic composition of seawater ($\delta^{11}\text{B}_{\text{sw}}$). This is

658 illustrated in Extended Data Fig 8. Here $p\text{CO}_2^{\text{atm}}$ is calculated from an artificial $\delta^{11}\text{B}$ and temperature
659 record (Extended Data Fig 8a), a TA of either 2000 $\mu\text{mol/kg}$, 2300 $\mu\text{mol/kg}$ or 2600 $\mu\text{mol/kg}$, a $\delta^{11}\text{B}_{\text{sw}}$
660 of 38.8, 39.6 (i.e. modern) or 40.4 ‰ (Extended Data Fig 8) and the assumption that $p\text{CO}_2^{\text{atm}} =$
661 $p\text{CO}_2^{\text{sw}}$. These parameter choices result in a large difference in absolute CO_2 but, although they are
662 extreme and perhaps unlikely for the Pliocene, the slope of a linear regression of global temperature
663 change and ΔF_{CO_2} is very similar for each set of parameters (Extended Data Fig 8c,d). So much so,
664 even with only a poor knowledge of $\delta^{11}\text{B}_{\text{sw}}$ (e.g. ± 0.8 ‰) and TA (e.g. ± 300 $\mu\text{mol/kg}$) the accuracy of
665 the relationship between reconstructed ΔF_{CO_2} and temperature is not unduly impacted.

666 The residence time of boron in seawater (10-20 Ma) ensures that changes in $\delta^{11}\text{B}_{\text{sw}}$ across the time
667 interval examined here (1 Myr) are unlikely to be large (<0.1 ‰; ref. 67) and so uncertainty in the
668 absolute value of $\delta^{11}\text{B}_{\text{sw}}$ and any changes across the study interval can be ignored for our
669 determinations of S^p . In all the previous calculations we assume that TA is randomly distributed
670 between 2155 and 2505 $\mu\text{mol/kg}$, therefore accounting for all possible trends in TA across the time
671 interval studied within this range. However, to better examine the influence of a large secular shift in
672 TA on our estimates of S^p we have imposed a 200 $\mu\text{mol/kg}$ decrease (TAd) or increase (TAi) across
673 our Pliocene study interval. The slope for the regressions using one parameter set (VDW11 and sea-
674 level from ref. 46 recalculated by ref. 12) but with such a varying TA are shown in Extended Data Fig
675 8e&f. Even this relatively large secular change does not have a major influence on the estimated
676 slope, clearly illustrating that our assumptions regarding TA, both its absolute value and its secular
677 evolution, have little influence on our calculated ΔF_{CO_2} and hence our conclusions.

678 **Pliocene $p\text{CO}_2^{\text{atm}}$ variability** The apparent cyclicity in our Pliocene CO_2 record can be investigated
679 using spectral analysis. Extended Data Fig 4c shows the evolutive power spectra for the Pliocene
680 $p\text{CO}_2^{\text{atm}}$ and a ~ 100 kyr cycle is clearly dominant. Our sampling resolution is 1 sample ~ 13 kyr, which
681 is not sufficient to resolve cycles of a precessional length (e.g. 19 and 23 kyr) but may be adequate to
682 resolve obliquity (~ 41 kyr length) yet these cycles are apparently absent in the generated spectra

683 (Extended Data Fig 4c). To ensure our resolution is not biasing this result we have sampled the LR04
684 benthic $\delta^{18}\text{O}$ stack at our exact sampling resolution and examined the evolutive power spectra of
685 this sampled record (Extended Data Fig 4d). This analysis reveals the presence of 100 kyr and 41 kyr
686 cycles in the $\delta^{18}\text{O}$ data, despite our relatively low resolution, supporting the observation that the
687 dominant cycle in Pliocene $p\text{CO}_2^{\text{atm}}$ is ~ 100 kyr.

688 The magnitude of Pliocene $p\text{CO}_2^{\text{atm}}$ variability, shown in Extended Data Fig 4a, is similar to that
689 exhibited by published late and mid-Pleistocene $\delta^{11}\text{B}-p\text{CO}_2^{\text{atm}}$ records (green and red lines on
690 Extended Data Fig 4a) and by the Late Pleistocene ice core data when noise that is approximately
691 equivalent to our $\delta^{11}\text{B}-p\text{CO}_2^{\text{atm}}$ uncertainty is added ($\pm 35 \mu\text{atm}$; black dashed line on Extended Data
692 Fig 4a). In contrast, the $\delta^{18}\text{O}$ variability for these time intervals increases markedly from the
693 Pliocene to late Pleistocene as the magnitude of glacial-interglacial cycles increases (Fig 1e, Extended
694 Data Fig 4b).

695

696 **References (for Methods only)**

697 51 Lawrence, K.T., Sigman, D.M., Herbert, T.M., Riihimaki, C.A., Bolton, C.T., Martinez-Garcia, A.,

698 Rosell-Mele, A., and Haug, G. Time-transgressive productivity changes in the North Atlantic

699 upon Northern Hemisphere glaciation, *Paleoceanography*, 28, doi: 10.1002/2013PA002546

700 (2013).

701 52 Barker, S., Greaves, M., Elderfield, H. A study of cleaning procedures used for foraminiferal Mg/Ca

702 paleothermometry. *Geochemistry, Geophysics, Geosystems*, 4(9): 8407,

703 doi:10.1029/2003GC000559 (2003).

704 53 Yu, J., Elderfield, H., Greaves, M., Day, J. Preferential dissolution of benthic foraminiferal calcite

705 during laboratory reductive cleaning. *Geochemistry Geophysics Geosystems*, Q06016:

706 doi:10.1029/2006GC001571 (2007).

707 54 Rae, J.W.B., Foster, G.L., Schmidt, D.N., Elliott, T. Boron isotopes and B/Ca in benthic foraminifera:
708 proxies for the deep ocean carbonate system. *Earth and Planetary Science Letters*, 302: 403-
709 413 (2011).

710 55 Medina-Elizalde, M., Lea, D.W., Fantle, M.S. Implications of seawater Mg/Ca variability for Plio-
711 Pleistocene tropical climate reconstruction. *Earth and Planetary Science Letters*, 269, 584-594
712 (2008).

713 56 Evans, D., Muller, W. Deep time foraminifera Mg/Ca paleothermometry: Nonlinear correction for
714 secular change in seawater Mg/Ca. *Paleoceanography*, 27, PA4205, (2012).

715 57 Fantle, M.S., DePaolo, D.J. Sr isotopes and pore fluid chemistry in carbonate sediment of the
716 Ontong Java Plateau: Calcite recrystallisation rates and evidence for a rapid rise in seawater
717 Mg over the last 10 million years. *Geochim.Cosmochim. Acta* 70: 3883-3904 (2006).

718 58 Delaney, M. L., WH Bé, A. & Boyle, E. A. Li, Sr, Mg, and Na in foraminiferal calcite shells from
719 laboratory culture, sediment traps, and sediment cores. *Geochim.Cosmochim. Acta* 49, 1327-
720 1341 (1985).

721 59 Dekens, P.S., Lea, D.W., Pak, D.K., Spero, H.J. Core top calibration of Mg/Ca in tropical
722 foraminifera: Refining paleotemperature estimation. *Geochemistry, Geophysics, Geosystems*
723 (G3), 3(4): doi: 10.1029/2001GC000200 (2002).

724 60 Catanzaro, E.J. et al. Boric assay; isotopic, and assay standard reference materials. US National
725 Bureau of Standards, Special Publication, 260-17, 70 pp (1970).

726 61 Klochko, K., Kaufman, A.J., Yoa, W., Byrne, R.H., Tossell, J.A. Experimental measurement of boron
727 isotope fractionation in seawater. *Earth and Planetary Science Letters*, 248: 261-270 (2006).

728 62 Hemming, N.G., Hanson, G.N. Boron isotopic composition and concentration in modern marine
729 carbonates. *Geochimica et Cosmochimica Acta*, 56: 537-543 (1992).

730 63 Hemming, N.G., Reeder, R.J., Hanson, G.N., 1995. Mineral-fluid partitioning and isotopic
731 fractionation of boron in synthetic calcium carbonate. *Geochimica et Cosmochimica Acta*,
732 59(2): 371-379 (1995).

733 64 Dickson, A. G. Thermodynamics of the dissociation of boric-acid in synthetic seawater from
734 273.15 to 318.15 K. *Deep-Sea Res.* **37**, 755-766 (1990).

735 65 Foster, G.L., Pogge von Strandmann, P.A.E., Rae, J.W.B. Boron and magnesium isotopic
736 composition of seawater. *Geochemistry Geophysics Geosystems*, 11(8): Q08015,
737 doi:10.1029/2010GC003201 (2010).

738 66 Herbert, T.D., Cleaveland Peterson, L., Lawrence, K.T., Liu, Z. Tropical Ocean Temperatures Over
739 the Past 3.5 Million Years. *Science*, 328: 1530-1534 (2010).

740 67 Lemarchand, D., Gaillardet, J., Lewin, E., Allegre, C.J. Boron isotope systematics in large rivers:
741 implications for the marine boron budget and paleo-pH reconstruction over the Cenozoic.
742 *Chemical Geology*, 190: 123-140 (2002).

743 68 Foster, G.L., Lear, C.H., Rae, J.W.B. The evolution of pCO₂, ice volume and climate during the
744 middle Miocene. *Earth and Planetary Science Letters*, 341-344: 243-254 (2012).

745 69 Raitzsch, Hönisch, B. Cenozoic boron isotope variations in benthic foraminifers. *Geology*, 41(5):
746 591-594 (2013).

747 70 Zeebe, R., Wolf-Gladrow, D.A. CO₂ in Seawater: Equilibrium, Kinetics, Isotopes. Elsevier
748 Oceanography Series 65. Elsevier, Amsterdam, 346 pp (2001).

749 71 R Core Team, R: A language and environment for statistical computing. R Foundation for
750 Statistical Computing, Vienna, Austria. ISBN 3-900051-07-0, URL <http://www.R-project.org/>
751 (2013).

752 72 Tyrrell, T., Zeebe, R.E. History of carbonate ion concentration over the last 100 million years.
753 *Geochimica et Cosmochimica Acta*, 68(17): 3521-3530 (2004).

754 73 Clark, P.U. et al. The middle Pleistocene transition: characteristics, mechanisms, and implications
755 for long-term changes in pCO₂. *Quaternary Science Reviews*, 25: 3150-3184 (2006).

756 74 Foster, G. L. et al. Interlaboratory comparison of boron isotope analyses of boric acid, seawater
757 and marine CaCO₃ by MC-ICPMS and NTIMS. *Chemical Geology* 358, 1-14,
758 doi:<http://dx.doi.org/10.1016/j.chemgeo.2013.08.027> (2013).

- 759 75 Bolton, C. T., Stoll, H. M., Mendez-Vicente, A. Vital effects in coccolith calcite: Cenozoic climate-
760 pCO₂ drove the diversity of carbon acquisition strategies in coccolithophores?
761 *Paleoceanography* 27 (2012).
- 762 76 Zachos, J., Pagani, M., Sloan, L., Thomas, E., Billups, K. Trends, rythms, and aberrations in global
763 climate 65 Ma to present. *Science*, 292: 686-693 (2001).
- 764 77 Müller, P. J., Kirst, G., Ruhland, G., Von Storch, I. & Rosell-Melé, A. Calibration of the alkenone
765 paleotemperature index UK'37 based on core-tops from the eastern South Atlantic and the
766 global ocean (60 N-60 S). *Geochim. Cosmochim. Acta* 62, 1757-1772 (1998).
- 767 78 Lawrence, K.T., Herbert, T.D., Brown, C.M., Raymo, M.E., Haywood, A.M. High-amplitude
768 variations in North Atlantic sea surface temperature during the early Pliocene warm period.
769 *Paleoceanography*, 24(PA2218): doi: 10.1029/2008PA001669 (2009).
- 770 79 Lawrence, K.T., Sosdian, S., White, J.M., Rosenthal, Y. North Atlantic climate evolution through
771 the Plio-Pleistocene climate transistions. *Earth and Planetary Science Letters*, 300: 329-342
772 (2010).
- 773 80 Brierley, C.M. et al. Greatly expanded tropical warm pool and weakened Hadley Circulation in the
774 Early Pliocene. *Science*, 323: 1714-1718 (2009).
- 775 81 Etourneau, J., Martinez, P., Blanz, T., Schneider, R. Pliocene-Pleistocene variability of upwelling
776 activity, productivity, and nutrient cycling in the Benguela Region. *Geology*, 37(10): 871-874
777 (2009).
- 778 82 Etourneau, J., Schneider, R., Blanz, T., Martinez, P. Intensification of the Walker and Hadley
779 atmospheric circulations during the Pliocene-Pleistocene climate transition. *Earth and*
780 *Planetary Science Letters*, 297: 103-110 (2010).
- 781 83 Lawrence, K.T., Liu, Z., Herbert, T.D. Evolution of the Eastern Tropical Pacific Through Plio-
782 Pleistocene Glaciation. *Science*, 312: 79-83 (2006).

783 84 Martinez-Garcia, A., Rosell-Melé, A., McClymont, E.L., Gersonde, R., Haug, G.H. Subpolar link to
784 the emergence of the modern equatorial Pacific cold tongue. *Science*, 328: 1550-1553
785 (2010).

786 85 Dekens, P. S., Ravelo, A. C. & McCarthy, M. D. Warm upwelling regions in the Pliocene warm
787 period. *Paleoceanography* 22 (2007).

788 86 Rayner, N. A. et al. Global analyses of sea surface temperature, sea ice, and night marine air
789 temperature since the late nineteenth century. *Journal of Geophysical Research:*
790 *Atmospheres* 108, 4407, doi:10.1029/2002jd002670 (2003).

791 87 Kennedy, J.J., Rayner, N.A., Smith, R.O., Parker, D.E., Saunby, M. Reassessing biases and other
792 uncertainties in sea surface temperature observations in situ since 1850: 1. Measurement
793 and sampling uncertainty. *Journal of Geophysical Research*, 116, D14103:
794 doi:10.1029/2010JD015218 (2011a).

795 88 Kennedy, J.J., Rayner, N.A., Smith, R.O., Parker, D.E., Saunby, M. Reassessing biases and other
796 uncertainties in sea surface temperature observations measured in situ since 1850: 2. Biases
797 and homogenization. *Journal of Geophysical Research*, 116, D14104, (2011b).

798 89 Waelbroeck, C. et al., Constraints on the magnitude and patterns of ocean cooling at the Last
799 Glacial Maximum. *Nature Geoscience*, 2: 127-132, (2009).

800 90 Efron, B. Bootstrap Methods: another look at the Jackknife. *Annals of Statistics*, 7: 1-26 (1979).

801 91 Locarnini, R. A. et al. World Ocean Atlas 2013, Volume 1: Temperature. NOAA Atlas NESDIS 73, 40
802 pp (2013).

803 92 Schlitzer, R., Ocean Data View, <http://odv.awi.de> (2012).

804 93 Siddall, M. et al. Sea-level fluctuations during the last glacial cycle. *Nature*, 423: 853-858 (2003).

805

806

807

808 **Figure Legends for Extended Data Figures**

809 **Extended Data Figure 1. Maps of modern mean annual $\Delta p\text{CO}_2$ and sea surface temperature**

810 **labelled with site locations.** (a) Map of sites used for $p\text{CO}_2^{\text{atm}}$ reconstruction with the mean annual
811 modern $\Delta p\text{CO}_2$ from the reconstruction of ref. 21. (b) Map of the sites (and labelled with their
812 depths) used to generate SSTst with mean annual modern SST from the World Ocean Atlas 2013 (ref.
813 91). Figures constructed and data visualised in Ocean Data View⁹².

814 **Extended Data Figure 2. Comparisons of boron isotope based- $p\text{CO}_2^{\text{atm}}$ estimates with other**

815 **methodologies and archives.** (a) Estimates of $p\text{CO}_2^{\text{atm}}$ from published $\delta^{11}\text{B}$ -records compared to ice-
816 core CO_2 (red line; ref. 27-29). The dotted line is for $p\text{CO}_2 = 278 \mu\text{atm}$. In (a) the data of ref. 20 (blue
817 circles) have been recalculated in the same manner as described here for the Pliocene, including
818 using the *G. ruber* $\delta^{11}\text{B}$ -pH calibration of ref. 18. Error band encompasses 68% (dark blue) and 95%
819 (light blue) of 10,000 Monte Carlo simulations of $p\text{CO}_2^{\text{atm}}$ (as described in text). Also shown are the
820 *G. sacculifer* based $\delta^{11}\text{B}$ - $p\text{CO}_2^{\text{atm}}$ record of ref. 30 (green circles). In this case error bars ($\pm 25 \mu\text{atm}$)
821 are as determined in that study. Despite similar analytical uncertainty, the smaller error bars for the
822 ref. 30 data result from these authors not propagating the $\delta^{11}\text{B}$ -pH calibration uncertainty and
823 considering a smaller range in temperature, salinity and alkalinity uncertainty than in this study (\pm
824 $0.76 \text{ }^\circ\text{C}$, $\pm 1 \text{ psu}$, $\pm 27 \mu\text{mol/kg}$ vs. $\pm 3 \text{ }^\circ\text{C}$, $\pm 3 \text{ psu}$, $\pm 175 \mu\text{mol/kg}$ with a flat probability in this study).
825 (b) $\delta^{11}\text{B}$ -based $p\text{CO}_2^{\text{atm}}$ record generated here (blue closed circles and 95% and 68% uncertainty
826 band) with $p\text{CO}_2^{\text{atm}}$ from the $\delta^{13}\text{C}$ of alkenones from published studies. See caption for Figure 1 for
827 details. (c) $\delta^{11}\text{B}$ -based $p\text{CO}_2^{\text{atm}}$ record generated here (blue closed circles and 95% and 68%
828 uncertainty band) with $p\text{CO}_2^{\text{atm}}$ from previous $\delta^{11}\text{B}$ -based studies and from plant stomata. See
829 caption for Figure 1 for details. (d – f) Comparison of cross plots of CO_2 forcing and ΔMAT for our
830 high resolution $\delta^{11}\text{B}$ - CO_2 record (d), published alkenone- CO_2 (e) and published low resolution $\delta^{11}\text{B}$ -
831 CO_2 (f). In each panel the slopes of regression lines fitted through the data are labelled ($\pm 1 \text{ se}$). In
832 (d) ice-core CO_2 are shown in red open circles and Pliocene $\delta^{11}\text{B}$ - CO_2 in open blue circles. In (e) and

833 (f) ice-core CO₂ data are shown in grey for clarity. In (e) alkenone-CO₂ data are from the following
834 sources: ODP 1208 (orange, ref. 16), ODP 806 (purple, ref. 16); ODP 925 (brown, ref. 49); ODP 999
835 (green circles = ref. 25; green squares = ref. 26). In (c) δ¹¹B-CO₂ are from ODP999 (blue²⁵ and red²³).

836 **Extended Data Figure 3. Probability density functions for equivalent aged samples from ODP Site**
837 **662 and ODP Site 999.** Each panel, labelled with age in ka, shows the probability density function for
838 a given estimate of pCO₂^{atm} from ODP Site 662 (red) and ODP Site 999 (blue). In most instances
839 equal age samples are compared, but in some cases either where variability is high and/or
840 equivalent age samples are absent, we show neighbouring samples from ODP Site 999 (e.g. bottom
841 left and right). This comparison indicates that although the mean pCO₂^{atm} of ODP 662 tends to be
842 higher than ODP 999, there is always significant overlap between the estimates from the two sites.

843 **Extended Data Figure 4. Probability density functions of pCO₂^{atm} and benthic δ¹⁸O and time series**
844 **analysis.** (a) Probability density functions (pdf) of the residuals of δ¹¹B-pCO₂^{atm} about the long-term
845 trend for the late Pliocene (this study; blue line), the mid-Pleistocene³⁰ (green line) and late-
846 Pleistocene^{19,20,21} (red line). Dashed vertical lines show the upper and lower limit (labelled in figure)
847 encompassing 90 % of the data. The residual of the ice-core CO₂ record²⁷⁻²⁹ about the long-term
848 mean for 0 – 0.8 Ma plus a random noise equivalent to ± 35 μatm (the typical δ¹¹B-CO₂ uncertainty)
849 is shown as a black dashed pdf. (b) Probability density functions of the residual of LR04 benthic δ¹⁸O
850 from the long-term trend for the late-Pleistocene (red), mid-Pleistocene (green) and late Pliocene
851 (blue). Dashed vertical lines show the upper and lower limit (labelled in figure) encompassing 90% of
852 the data. In contrast to the pCO₂^{atm}, δ¹⁸O clearly exhibits an increase in variability over the last 3.3
853 million years. (c) Evolutive power spectral analyses of Pliocene pCO₂^{atm} and resampled δ¹⁸O (d). The
854 evolutive power spectra was computed using the fast Fourier transform of overlapping segments
855 with a 300,000-year moving window. Before spectral analysis, all series were notch-filtered to
856 remove the long-term trend (bandwidth = 0.005), and interpolated to 12 kyr intervals (the real
857 resolution of our record is ~13.5 kyr).

858 **Extended Data Figure 5. Summary of sea-level records used to calculate ΔF_{L} .** In (a) and (b) the red
859 curve is from ref. 13 (R14) based on the planktic $\delta^{18}\text{O}$ from the Mediterranean Sea and the methods
860 developed for the Red Sea by ref. 89. We have removed those intervals identified as possible
861 Sapropel events and linearly interpolated across gaps in the original record. The black curve is the
862 sea-level record from an inversion of the benthic oxygen isotope record of ref. 72 (tuned to LR04
863 here) using an ice sheet model³⁵ (VDW11). The blue curve in (a) is based on the planktic/bulk $\delta^{18}\text{O}$
864 from the Red Sea⁴⁴ for the interval 0-520 ka and the paired Mg/Ca and benthic $\delta^{18}\text{O}$ from the deep
865 South Pacific for the interval 520-800 ka⁴⁵ (R09+E12). The green curve in (b) is based on a scaling of
866 the LR04 $\delta^{18}\text{O}$ stack to indicators of sea-level from sequence stratigraphy (ref. 46 recalculated by ref.
867 12). In each the uncertainty in the reconstruction at 95% confidence is shown by an appropriately
868 coloured error band. Marine isotope stages mentioned in text are labelled.

869 **Extended Data Figure 6. Stacked sea surface temperature record (SSTst).** (a) and (b) Number of
870 records that contribute to SSTst through time. (c) and (d) uncertainty in SSTst due to analytical
871 uncertainty (at 95% confidence; red band) and showing the influence of jackknifing (i.e. removing one
872 record at a time; grey lines show maximum and minimum). Note that the jackknifing illustrates that
873 no one record has undue influence on SSTst.

874 **Extended Data Figure 7. Comparison of global SST from HadSST3 dataset with SST HadISST1 from**
875 **ODP sites.** (a) Historic global mean annual sea surface temperature anomaly from the HadSST3
876 dataset⁸⁷⁻⁸⁸ (red circles) and mean SST at locations above the ODP sites that make up SSTst from
877 HadISST1 (blue; local SST). Thick red and blue lines are non-parametric smoothers through both
878 datasets. (b) Cross plot of global mean annual SST and local SST. The regression line determined
879 using linear regression has a slope of ~ 1 and intercept of close to 0, therefore, local SST captures the
880 global trend well. The shaded blue band in (b) represents the 95% confidence interval of the
881 regression line.

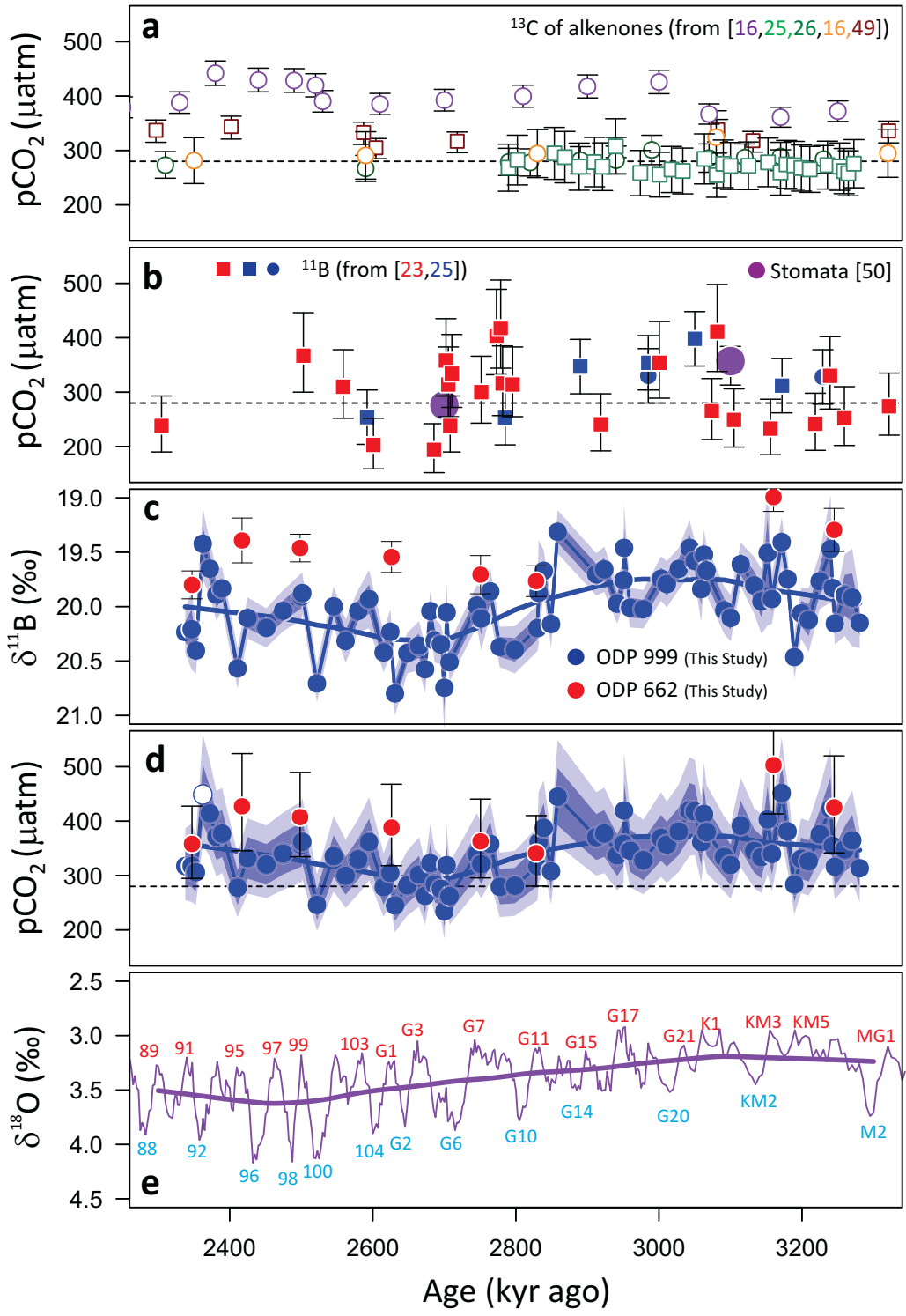
882 **Extended Data Figure 8. The influence of TA and $\delta^{11}\text{B}_{\text{sw}}$ on determinations of S^{p} using linear**
883 **regression.** Artificial $\delta^{11}\text{B}$ record (a) and temperature record (b). Cross plot and regressions of $\delta^{11}\text{B}$ -
884 ΔF_{CO_2} and global temperature for dramatically varying total alkalinity from 2000 to 2600 $\mu\text{mol}/\text{kg}$
885 (TA; c) and $\delta^{11}\text{B}_{\text{sw}}$ from 38.8 to 40.4 ‰ (d). The slopes of the regressions, which are very similar
886 regardless of parameter choice, are colour coded and listed in the bottom right hand corner of (c)
887 and (d). (e) Probability density function of slope for regressions of Pliocene-aged ΔMAT against
888 ΔF_{CO_2} and (f) $\Delta F_{\text{CO}_2, \text{LI}}$, where TA is decreasing by 200 (dashed) and increasing by 200 $\mu\text{mol}/\text{kg}$
889 (dotted). Note that despite large variations in TA the slope of the regressions do not change
890 significantly.

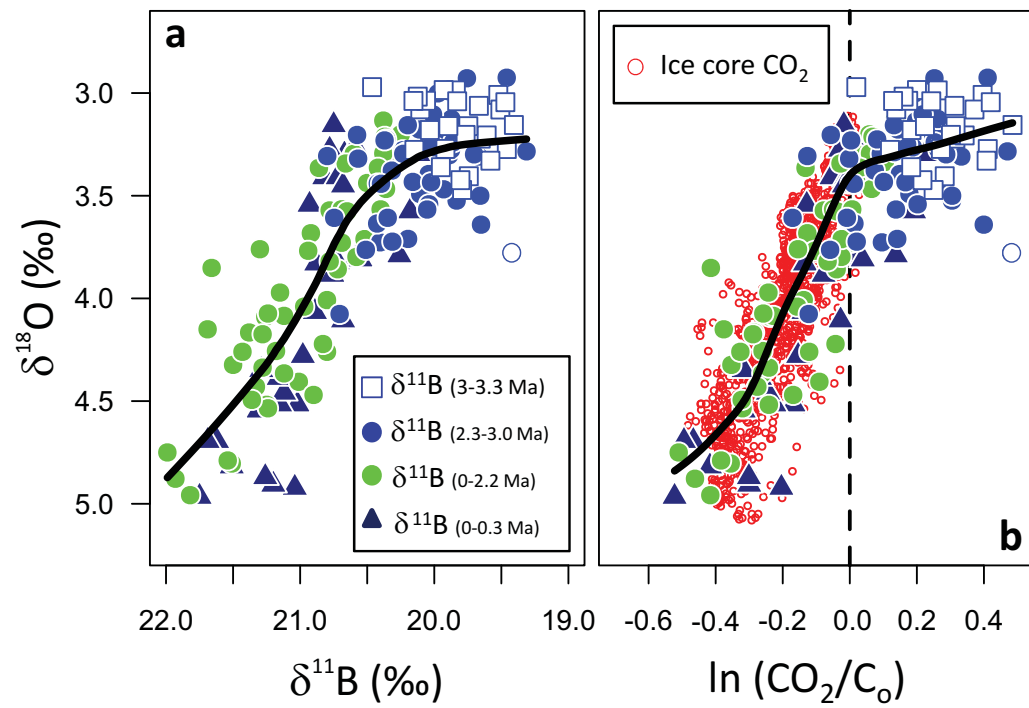
891

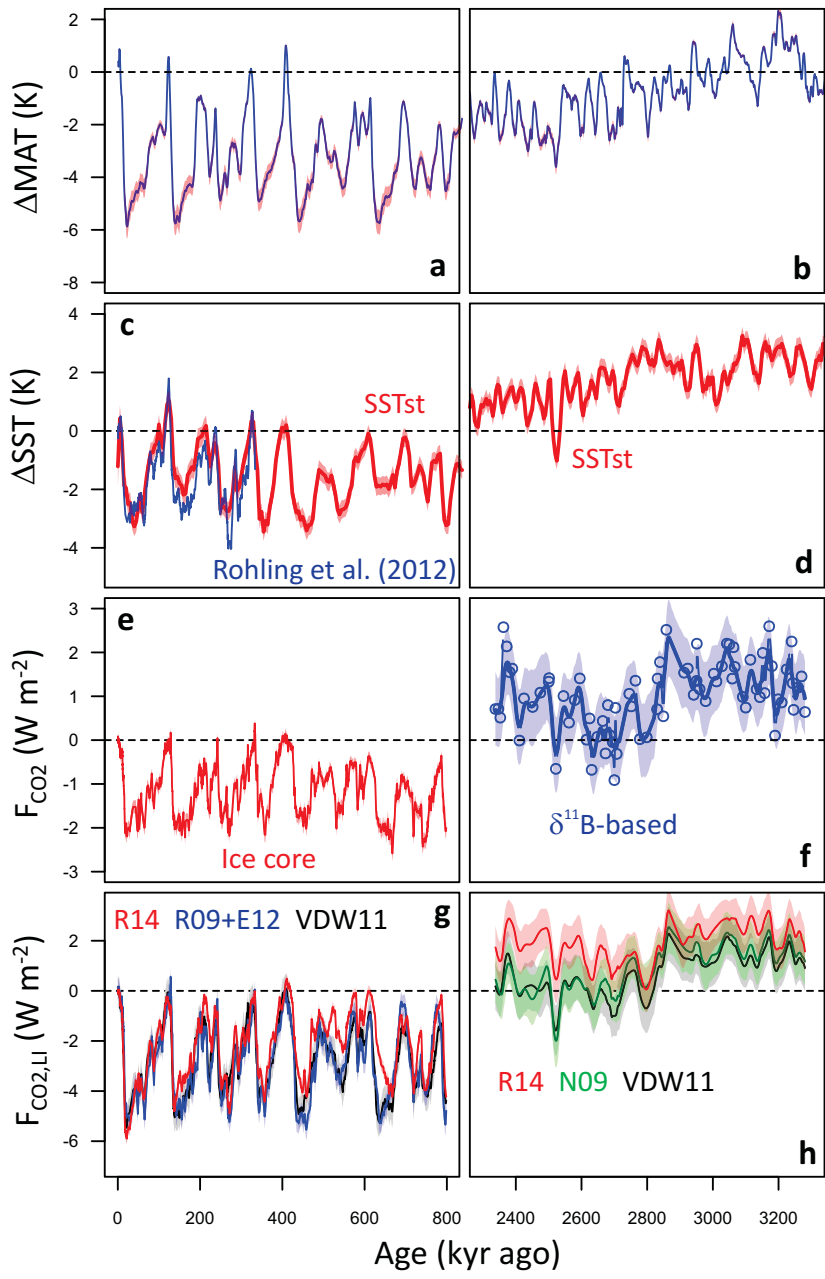
892

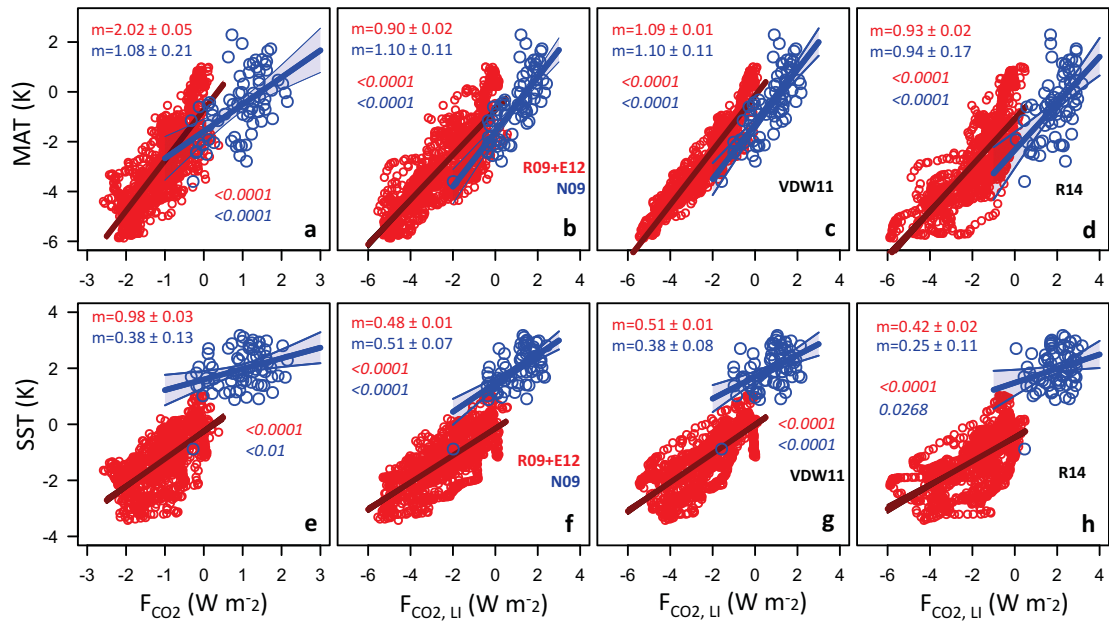
893

894









Global Temperature

Sea Surface Temperature

